Allosteric communication in Class A β-lactamases occurs via cooperative coupling of loop dynamics

Ioannis Galdadas[1†], Shen Qu[2†], Ana Sofia F Oliveira[3,4], Edgar Olehnovics[2], Andrew R Mack[5,6], Maria F Mojica[5,7], Pratul K Agarwal[8], Catherine L Tooke[9], Francesco L Gervasio[1,10,11], James Spencer[9], Robert A Bonomo[5,6,7,12,13,14,15], Adrian J Mulholland[3*], Shozeb Haider [2*]

***For correspondence:**
shozeb.haider@ucl.ac.uk (SH);
adrian.mulholland@bristol.ac.uk (AJM)

[†]These authors contributed equally to this work

[1]University College London, Department of Chemistry, London, United Kingdom; [2]University College London School of Pharmacy, Pharmaceutical and Biological Chemistry, London, United Kingdom; [3]University of Bristol, Centre for Computational Chemistry, School of Chemistry, Bristol, United Kingdom; [5]Veterans Affairs Northeast Ohio Healthcare System, Research Service, Cleveland, OH, USA; [6]Case Western Reserve University, Department of Molecular Biology and Microbiology, Cleveland, OH, USA; [7]Case Western Reserve University, Department of Infectious Diseases, School of Medicine, Cleveland, OH, USA; [8]Department of Physiological Sciences and High-Performance Computing Center, Oklahoma State University, Stillwater, OK, USA; [9]University of Bristol, School of Cellular and Molecular Medicine, Bristol, United Kingdom; [10]University College London, Institute of Structural and Molecular Biology, London, United Kingdom; [11]University of Geneva, Pharmaceutical Sciences, Geneva, Switzerland; [12]Case Western Reserve University, Department of Biochemistry, Cleveland, OH, USA; [13]Case Western Reserve University, Department of Pharmacology, Cleveland, OH, USA; [14]Case Western Reserve University, Department of Proteomics and Bioinformatics Cleveland, OH, USA; [15]CWRU-Cleveland VAMC Center for Antimicrobial Resistance and Epidemiology (Case VA CARES) Cleveland, OH, USA

Abstract Understanding allostery in enzymes and tools to identify it, offer promising alternative strategies to inhibitor development. Through a combination of equilibrium and nonequilibrium molecular dynamics simulations, we identify allosteric effects and communication pathways in two prototypical class A β-lactamases, TEM-1 and KPC-2, which are important determinants of antibiotic resistance. The nonequilibrium simulations reveal pathways of communication operating over distances of 30 Å or more. Propagation of the signal occurs through cooperative coupling of loop dynamics. Notably, 50% or more of clinically relevant amino acid substitutions map onto the identified signal transduction pathways. This suggests that clinically important variation may affect, or be driven by, differences in allosteric behavior, providing a mechanism by which amino acid substitutions may affect the relationship between spectrum of activity, catalytic turnover and potential allosteric behavior in this clinically important enzyme family. Simulations of the type presented here will help in identifying and analyzing such differences.

Introduction

The rise in antimicrobial resistance (AMR) is a growing global public health crisis (***Centers for Disease Control and Prevention (U.S.), 2019***). As AMR has continued to spread and many antimicrobial agents have become ineffective against previously susceptible organisms, the World Health Organization recently projected that AMR could result in up to 10 million deaths annually by 2050 (***on Antimicrobial Resistance, 2019***). The problem of AMR is particularly urgent given the alarming proliferation of antibiotic resistance in bacteria; pathogens associated with both community-acquired and healthcare-associated infections are increasingly resistant to first-line and even reserve agents (***Lythell et al., 2020***). This not only poses a serious challenge obstacle in fighting common and severe bacterial infections, but also reduces the viability and increases the risks of interventions such as orthopedic surgery and also threatens new antibiotics coming to the market (***Bush and Page, 2017***). AMR risks negating a century of progress in medicine made possible by the ability to effectively treat bacterial infections.

In spite of the advances in the field of antimicrobial chemotherapy, the efficacy, safety, chemical malleability and versatility of β-lactams, makes them the most prescribed class of antibiotics (***Tooke et al., 2019***). Their cumulative use exceeds 65% of all injectable antibiotics in the United States (***Bush and Bradford, 2016***). β-lactam antibiotics work by inhibiting penicillin-binding proteins (PBPs), a group of enzymes that catalyze transpeptidation and transglycosylation reactions that occur during the bacterial cell wall biosynthesis (***Tooke et al., 2019***). A damaged cell wall results in loss of cell shape, osmotic destabilization, and is detrimental for bacterial survival in a hypertonic and hostile environment (***Bonomo, 2017***). Of the four primary mechanisms by which bacteria resist β-lactam antibiotics, the most common and important mechanism of resistance in Gram-negative bacteria, including common pathogens such as *Escherichia coli* and *Klebsiella pneumoniae*, is the expression of β-lactamase enzymes (***Tooke et al., 2019***). These enzymes hydrolyze the amide bond in the β-lactam ring, resulting in a product that is incapable of inhibiting PBPs (***Palzkill, 2018***).

The Ambler system of classifying β-lactamase enzymes categorizes them, based on amino acid sequence homology, into classes A, B, C and D (***Ambler, 1980***; ***Bush and Jacoby, 2010***). While β-lactamases of classes A, C and D are serine hydrolases, class B enzymes are metalloenzymes that have one or more zinc ions at the active site (***Palzkill, 2013***). Class A enzymes are the most widely distributed and intensively studied of all β-lactamases (***Tooke et al., 2019***). The hydrolytic mechanism in class A (***Figure 1–Figure Supplement 1***), revealed by experiments and QM/MM modelling, is initiated by reversible binding of the antibiotic in the active site of the enzyme (formation of the Michaelis complex). This is followed by nucleophilic attack of the catalytic serine (Ser70) on the carbonyl carbon of the β-lactam ring, resulting in a high-energy acylated intermediate that quickly resolves, following protonation of the β-lactam nitrogen and cleavage of the C-N bond, to a lower energy covalent acyl enzyme complex (***Chudyk et al., 2014***; ***Hermann et al., 2003***, ***2005***). Next, an activated water molecule attacks the covalent complex, leading to the subsequent hydrolysis of the bond between the β-lactam carbonyl and the serine oxygen, resulting in the regeneration of the active enzyme and release of the inactive β-lactam antibiotic (***Tooke et al., 2019***; ***Bonomo, 2017***; ***Palzkill, 2018***; ***Chudyk et al., 2014***; ***Fisher and Mobashery, 2009***; ***Hermann et al., 2006***; ***Hirvonen et al., 2019***; ***Pan et al., 2017***).

TEM-1 is one of the most common plasmid-encoded β-lactamases in Gram-negative bacteria and is a model class A enzyme (***Brown et al., 2009***). It has a narrow spectrum of hydrolytic activity that is limited to penicillins and early generation cephalosporins; in contrast, its activity towards large, inflexible, broad-spectrum oxyimino-cephalosporins such as the widely used antibiotic ceftazidime is poor (***Palzkill, 2018***). However, mutations in the $bla_{\text{TEM-1}}$ gene have led to amino acid modifications, which allow subsequent TEM-1 variants to hydrolyze broad-spectrum cephalosporins (so-called 'extended-spectrum' activity) or to avoid the action of mechanism-based inhibitors such as clavulanate that are used in combination with β-lactams to treat β-lactamase producing organisms (***Brown et al., 2009***). Another class A enzyme, KPC-2 (*Klebsiella pneumoniae*

carbapenemase-2) encoded by the bla_{KPC-2} gene is an extremely versatile β-lactamase (***Queenan et al., 2004***) with a broad spectrum of substrates that includes penicillins, cephamycins and, importantly, carbapenems (***Queenan et al., 2004***; ***Yigit et al., 2003***). Currently, predominant strains of *Klebsiella pneumoniae* and other *Enterobacterales* continue to be identified as responsible for outbreaks internationally. Continued dissemination of KPC makes this one of the β-lactamases of most immediate clinical importance and a key target for inhibitor development.

The structure and activity of Class A β-lactamases have been well studied (***Palzkill, 2018***; ***Papp-Wallace et al., 2012***; ***Salverda et al., 2010***). In spite of sequence differences, class A β-lactamases share the same structural architecture (***Philippon et al., 2016***), as evident from the present 47 structures of TEM-1 and 38 structures of KPC-2, or their engineered variants, deposited in the PDB at the time of this writing. However, despite the wide variety of substrates that TEM-1 and KPC-2 can hydrolyze, their structures are quite rigid. The average mean order parameter, S^2, as calculated from NMR experiments for TEM-1, is between 0.81-0.94 and almost all class A β-lactamases are conformationally identical (***Gobeil et al., 2019***; ***Morin and Gagné, 2009***; ***Savard and Gagné, 2006***). Loops (e.g. active site loops) play a crucial role in the activity of many enzymes (***Liao et al., 2018***), including β-lactamases. There is increasing evidence that active site conformations may be influenced by distal loops, connected e.g. through active closure and desolvation, and potentially via networks of coupled motions (***Liao et al., 2018***; ***Agarwal, 2019***; ***Bunzel et al., 2020***, ***2021***). The active sites of TEM-1 and KPC-2 are surrounded by three loops: (a) the Ω loop (residues 172-179), (b) the loop between α3 and α4 helices, in which a highly conserved aromatic amino acid is present at position 105 and (c) the hinge region, which lies opposite to the Ω loop and contains the α11 helix turn (***Figure 1***, ***Figure 1–Figure Supplement 2***). Two highly conserved residues, Glu166 and Asn170, which are essential for catalysis, influence the conformation of the Ω loop (***Banerjee et al., 1998***). The conformational dynamics of these loops play an important role in enzyme activity, and are probably modulated by evolution (***Pan et al., 2017***; ***Banerjee et al., 1998***; ***Escobar et al., 1994***; ***Guillaume et al., 1997***; ***Leung et al., 1994***; ***Zawadzke et al., 1996***). For example, we have recently found that differences in the spectrum of activity between KPC-2 and KPC-4 are due to changes in loop behavior (***Tooke et al., 2021***).

There has been extensive discussion about the possible contribution of protein dynamics to enzyme catalysis (***Glowacki et al., 2012***; ***Kamerlin and Warshel, 2010***; ***Luk et al., 2013***; ***Singh et al., 2015***). In some enzymes, conformational changes have been identified as necessary in preparing the system for reaction (***Liao et al., 2018***; ***Agarwal, 2019***). Several simulation studies, including long timescale and enhanced sampling molecular dynamics (MD) simulations and QM/MM simulations of reactions have been reported for TEM-1 and KPC-2 β-lactamases (***Chudyk et al., 2014***; ***Hirvonen et al., 2019***; ***Bowman et al., 2015***; ***Galdadas et al., 2018***; ***Hart et al., 2016***; ***Tooke et al., 2021***). MD simulations have explored cryptic pocket formation (***Hart et al., 2016***), studied protein-ligand interactions (***Fisette et al., 2012***), predicted antibiotic resistance (***Chudyk et al., 2014***; ***Hirvonen et al., 2019***; ***Galdadas et al., 2018***), explained the effects of mutations on enzyme specificities (***Zaccolo and Gherardi, 1999***), and investigated conserved hydrophobic networks (***Galdadas et al., 2018***). It remains a challenge to directly link conformational heterogeneity and function.

Understanding conformational behavior is relevant to β-lactamase inhibition as well as catalytic mechanism. For organisms producing class A β-lactamases co-administration of susceptible β-lactams with mechanism-based covalent inhibitors (e.g. clavulanate) represents a proven therapeutic strategy and has successfully extended the useful lifetime of penicillins in particular (***Fritz et al., 2018***; ***Drawz and Bonomo, 2010***). However, while the mechanism of direct inhibition by covalently bound inhibitors is well established (***Fritz et al., 2018***), the possibility of exploiting sites remote from the active center in allosteric inhibition strategies is less well explored, and where this has been achieved (***Horn and Shoichet, 2004***; ***Pemberton et al., 2019***; ***Hart et al., 2016***) the structural changes occurring as a result of ligand binding or unbinding to allosteric sites, and the relay of structural communication that leads to inhibition are not well understood. The conformational rearrangements that take place upon ligand (un)binding in allosteric sites and their potential

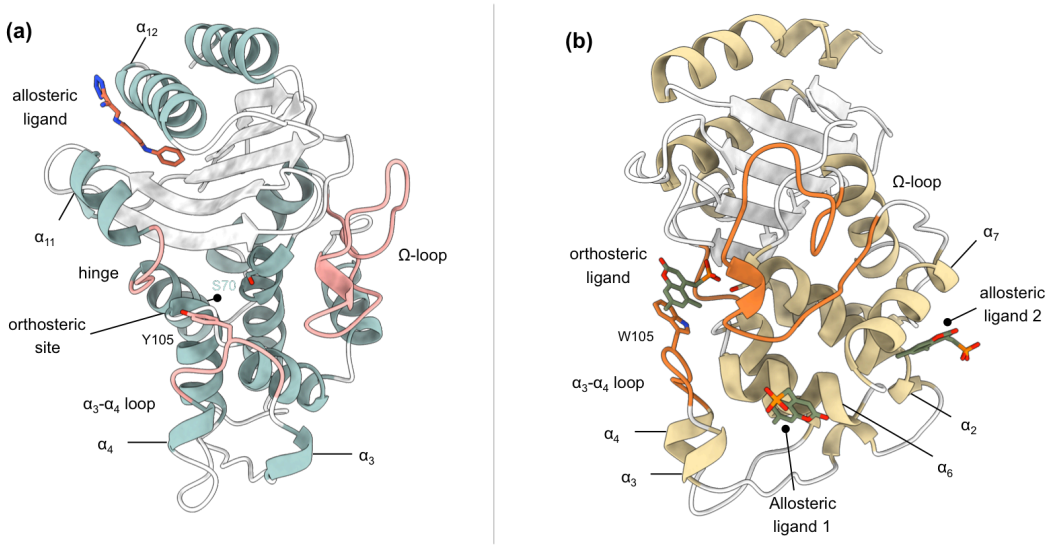

Figure 1. Crystal structures of (a) TEM-1 (PDB id 1PZP) and (b) KPC-2 (PDB id 6D18) -lactamases in complex with ligands bound to allosteric and the orthosteric sites. The helices around the allosteric binding sites and the loops that define the orthosteric binding site are highlighted. In case of KPC-2, allosteric ligand 2 is the site investigated here. See Table S1 for structural nomenclature.

Figure 1–Figure supplement 1. Catalytic cycle of a class A β-lactamase illustrated on the core structure of penicillins.

Figure 1–Figure supplement 2. Naming of the loops based on the secondary structure it connects.

connection to the β-lactamase active site, are the focus of this study.

Here, we employ a combination of equilibrium and nonequilibrium MD simulations to identify and study the response of two class A β-lactamases, namely TEM-1 and KPC-2, to the (un)binding of ligands at sites distant from the active site. Nonequilibrium simulations applying the Kubo-Onsager approach (***Ciccotti and Ferrario, 2016***; ***Ciccotti et al., 1979***) are emerging as an effective way to characterize conformational changes and communication networks in proteins (***Abreu et al., 2020***; ***Damas et al., 2011***; ***Oliveira et al., 2019a***,b).

To the best of our knowledge, this is the first application of this nonequilibrium MD approach to study enzymes. We study β-lactamases, whose ultrafast turnover rates can approach the diffusion limits for natural substrates (~10^7-10^8 $M^{-1}s^{-1}$) (***Fisher and Mobashery, 2009***). We perform 10 μs of equilibrium MD simulations of TEM-1 and KPC-2, with and without ligands present in their allosteric binding sites. These simulations identify conformational changes in the highly dynamic loops that shape the active site and structurally characterize the dynamics of the formation and dissolution of the allosteric pocket. We also carry out an extensive complementary set of 1600 short nonequilibrium MD simulations (a total of 8 μs of accumulated time), which reveal the response of the enzyme to perturbation and identify pathways in the enzymes that connect the allosteric site to other parts of the protein. These simulations demonstrate direct communication between the allosteric sites and the active site. The results show that this combination of equilibrium and nonequilibrium MD simulations offers a powerful tool and a promising approach to identify allosteric communication networks in enzymes.

Results

Equilibrium simulations of Apo_{EQ} and IB_{EQ} states

To explore the conformational space of TEM-1 and KPC-2 in the Apo_{EQ} (no ligand) and IB_{EQ} (inhibitor bound) states, we started by running a set of equilibrium simulations (20 replicas of 250 ns each)

that resulted in 5 μs of accumulated simulation time per system. Conformational changes during the simulations were assessed using their Cα root mean-squared deviation (RMSD) profiles (***Figure 2–Figure Supplement 2***). The simulated systems were considered equilibrated beyond 50 ns as shown by RMSD convergence. In each case, the proteins remained close to their initial conformation during the course of 250 ns (***Figure 2–Figure Supplement 2***a). The average RMSD for Apo_{EQ} and IB_{EQ} states were between 0.10-0.12 nm for all systems (***Figure 2–Figure Supplement 6***). The low RMSD values are consistent with previously published results, which have also shown class A β-lactamase enzymes to be largely rigid and conformationally stable when studied on long time scales and rarely divergent from the initial structure (***Gobeil et al., 2019***; ***Galdadas et al., 2018***). Conventional RMSD fitting procedure using all Cα atoms failed to separate regions of high versus low mobility. To resolve such regions, we used a fraction (%) of the Cα atoms for the alignment. Beyond this fraction, there is a sharp increase in the RMSD value for the remainder of the Cα atoms (***Figure 2–Figure Supplement 2***b). At 80%, the core of TEM-1 could be superimposed to less than 0.064 nm and 0.074 nm for Apo_{EQ} and IB_{EQ} states, respectively (***Figure 2–Figure Supplement 2***bi).

In the KPC-2 Apo_{EQ} state, the RMSD of 80% of the Cα atoms was below 0.060 nm, while the same subset of atoms had an RMSD below 0.066 nm in the IB_{EQ} state (***Figure 2–Figure Supplement 2***bii). This 80% fraction of Cα atoms constitutes the core of the enzyme and did not show any divergence from the initial reference structure (***Figure 2–Figure Supplement 2***c). RMSD values for the remaining 20% of Cα atoms varied between 0.16 to 0.23 nm. This apparent rigidity is consistent with the experimental finding, based upon e.g. thermal melting experiments ***Mehta et al.*** (***2015***), that KPC-2 is more stable than many other class A β-lactamases such as TEM-1. Some large conformational changes were observed in all replicates; these involved changes in conformations of the loops that connect secondary structural elements (***Figure 2–Figure Supplement 3***). To further validate the stability of the two systems, we analyzed structural properties including the radius of gyration (Rg; Figure S5), solvent accessible surface area (SASA; ***Figure 2–Figure Supplement 5***) and the secondary structure of each enzyme over the simulated time (***Figure 2–Figure Supplement 7***). The values for these properties are listed in ***Figure 2–Figure Supplement 6***.

Ligand-induced structural and dynamical changes

A ligand that binds to an allosteric site can control protein function by affecting the active site (***Laskowski et al., 2009***). This generally occurs by altering the conformational ensemble that the protein adopts (***Laskowski et al., 2009***; ***Motlagh et al., 2014***). To probe how ligand binding to an allosteric site affects the dynamics of β-lactamases, we calculated the Cα root mean-square fluctuation (RMSF) for both Apo_{EQ} and IB_{EQ} states. Higher RMSF values correspond to greater flexibility during the simulation. Although the Cα RMSF profiles for Apo_{EQ} and IB_{EQ} states are similar, indicating similar dynamics, there are some discernible differences (***Figure 2***).

In equilibrium simulations of TEM-1 and KPC-2, the hydrophobic core of the enzyme is stable and shows limited fluctuations. Most of the RMSF variance is observed in loops that connect secondary structural elements (***Figure 2***). In TEM-1 IB_{EQ}, higher fluctuations are observed predominantly in three distinct regions when compared with the Apo_{EQ} enzyme; in the loops between helices α7 and α8 (residues 155-165), α9 and α10 (residues 196-200) and the hinge region including helix α11 (residues 213-224) (***Figure 2***A). The α11 and the α12 helices are part of a highly hydrophobic region that also constricts the allosteric pocket in all TEM-1 apo crystal structures. Binding of the ligand disrupts the hydrophobic interactions within this region, resulting in the opening of the allosteric pocket between helices α11 and α12 ***Horn and Shoichet*** (***2004***).

It should be noted that the starting Apo_{EQ} structure of TEM-1 was generated from the IB crystal structure, by the removal of the ligand from the allosteric binding site. During the Apo_{EQ} simulations, α12 helix behaves like a lid and closes over the empty, hydrophobic, allosteric binding site, and thus displays high RMSF at the C-terminal end of the enzyme. This conformational change recovers the structure of the apo crystal form, as observed e.g. in PDB id 1ZG4 (***Stec et al., 2005***), as reflected to the RMSD of ~0.07 nm after superposition of the structures. The rest of the loops

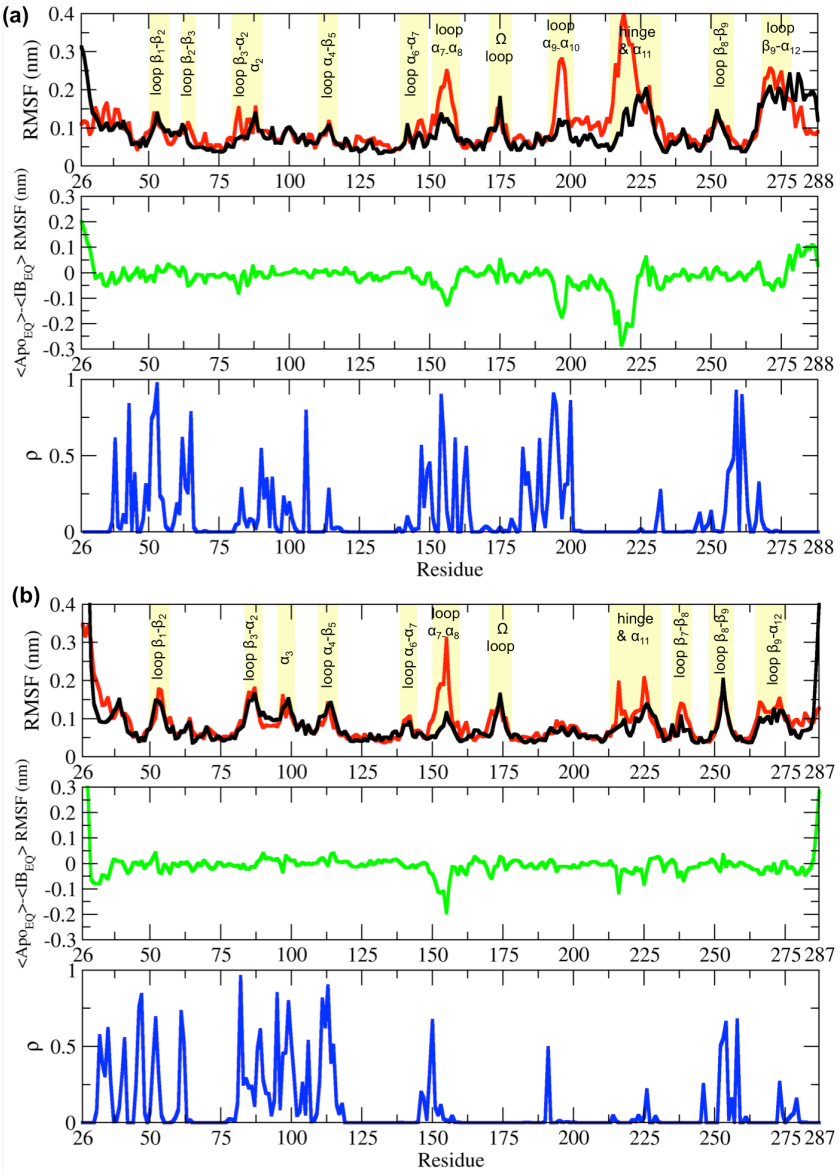

Figure 2. RMSF differences between the Apo_{EQ} and IB_{EQ} states of the (a) TEM-1 and (b) KPC-2 systems. The average change in RMSF in the Apo_{EQ} (black), the IB_{EQ} (red), the difference Apo_{EQ}-IB_{EQ} (green), and the associated ρ value (blue) is illustrated. The ρ values were obtained by conducting a Student's t-test to compare Apo_{EQ} and IB_{EQ} systems and to assess the significance of the differences.

Figure 2–Figure supplement 1. Schematic description of the long equilibrium (EQ) and short nonequilibrium (NE) simulations.

Figure 2–Figure supplement 2. Time series of the Cα Root Mean Squared Deviation (RMSD) of TEM-1 Apo_{EQ}, TEM-1 IB_{EQ}, KPC-2 Apo_{EQ} and KPC-2 IB_{EQ} systems, measured over the course of the 250 ns of each replica.

Figure 2–Figure supplement 3. Core Cα RMSD superimposition from TEM-1 and KPC-2 IB_{EQ} simulations.

Figure 2–Figure supplement 4. Time evolution of the radius of gyration (Rg) over the course of the 250 ns of each replicate.

Figure 2–Figure supplement 5. Solvent accessible surface area (SASA) over the course of the 250 ns of each replicate.

Figure 2–Figure supplement 6. Dynamical properties (RMSD, Rg and SASA) used to assess structural stability of the systems over the course of the equilibrium simulation.

Figure 2–Figure supplement 7. Probability to find each residue in a coil, helix, or strand over the course of the 250 ns of each replicate.

displayed comparable fluctuations in both Apo_{EQ} and IB_{EQ} states.

The differences between the Apo_{EQ} and IB_{EQ} states were of similar magnitude in KPC-2. In KPC-2 IB_{EQ}, more extensive fluctuations than in Apo_{EQ} were also observed in the loops between α7-α8 (residues 156-166), the hinge region, around α11 (residues 214-225) and in the loop between β7-β8 (residues 238-243) (***Figure 2***b). Conversely, fluctuations are slightly higher in the Apo_{EQ} than IB_{EQ} state in the loop leading into the Ω loop from α7 helix (residues 156-166). Overall, however, RMS fluctuations are similar in analogous regions of the IB_{EQ} and Apo_{EQ} states in both TEM-1 and KPC-2, highlighting the conservation of structural dynamics in class A β-lactamases. However, there were some fluctuations that were unique and limited to each enzyme (***Figure 2***).

In both TEM-1 and KPC-2 IB_{EQ} states, interactions of the ligands in their respective allosteric binding sites contribute to enhanced fluctuations (i.e. larger than in the Apo forms) of the local structural elements (***Figure 3–Figure Supplement 1***). The sites in which the ligands bind are very different. In TEM-1, the binding site is deep and forms a hydrophobic cleft. The ligand penetrates to the core of the enzyme and is sandwiched between helices α11 and α12 (***Horn and Shoichet, 2004***). The FTA ligand remains tightly bound in the allosteric pocket throughout the simulations (***Figure 3–Figure Supplement 2***).

In KPC-2, the allosteric binding site is shallow and solvent-exposed even in the absence of the ligand. Although the distal end of the pocket is hydrophobic, there are some polar amino acids on the proximal surface (e.g. Arg83 and Gln86), which are exposed to the solvent. This shallow site forms a part of a larger pocket that is occluded by the side chain of Arg83 (α7 helix). In some of our IB_{EQ} simulations, the Arg83 side chain rotates, leading to the opening of a larger hidden pocket. This enlarged space is now accessible to the ligand for exploring various interactions. The tumbling of GTV increases the fluctuations in the complex (***Figure 3–Figure Supplement 1***c,d), however, the ligand does not leave the binding site (***Figure 3–Figure Supplement 2***).

To further highlight the structural changes occurring as a result of ligand binding, positional C deviations were calculated between IB_{EQ} and Apo_{EQ} systems for the equilibrated part of the simulations (***Figure 3***a,b). The Cα deviation values plotted are an average between simulation taken by combining all trajectories from Apo_{EQ} and IB_{EQ} simulations for that particular system. This is one of the simplest approaches, which can determine residues undergoing largest structural rearrangements. The averaged Cα positional deviations are mapped onto the averaged Apo_{EQ} structure to visualize the largest relative displacements in three-dimensions (***Figure 3***c,d).

The hydrophobic cores of both TEM-1 and KPC-2 β-lactamase enzymes show little or no conformational change. The major differences between the Apo_{EQ} and IB_{EQ} states are in the loops connecting different secondary structure elements. In TEM-1, Cα deviations are observed in the loops between α4-β5 (residues 112-116), α7-α8 (residues 155-166), Ω loop (residue 172-179), α9-α10 (residue 196-200), hinge and α11 (residues 213-224), β7-β8 (residues 238-243) and β9-α12 (residues 267-272). There are some relatively minor deviations observed in loops β1-β2 (residues 51-55), β2-β3 (residues 61-65), α2-β4 (residue 86-93), α6-α7 (residues 143-144), β8-β9 (residues 252-258) and at the pivot of the α3 helix (residues 98-101). The hinge region and residues in helices α11 and α12 display the largest deviations. This is also in agreement with other experimental data that indicate the connection between the active site and the allosteric pocket studied in TEM-1 in the presence of BLIP inhibitor, seems to be mostly due to hinge region motions (***Meneksedag et al., 2013***).

The structural dynamics observed in KPC-2 were slightly different from TEM-1. In KPC-2, prominent C deviations were observed in the loops between β1-β2 (residues 51-55), α2-β4 (residue 88-93), α4-β5 (residues 114-116), α7-α8 (residues 156-166), Ω loop (residue 172-179), β7-β8 (residues 238-243), β8-β9 (residues 252-258), in the loop between β4-α3 leading up to the proximal end of α3 (residues 94-102) and in the hinge/α11 helix (residues 214-225). There are some minor deviations observed in α1-β1 (residues 39-42) and β9-α12 (residues 266-270). The most important ligand-induced Cα deviation is observed in the loop connecting the α4 helix to the β5 strand (residues 114-116). The deviation of the α4-β5 loop together with the deviation observed in the loop between

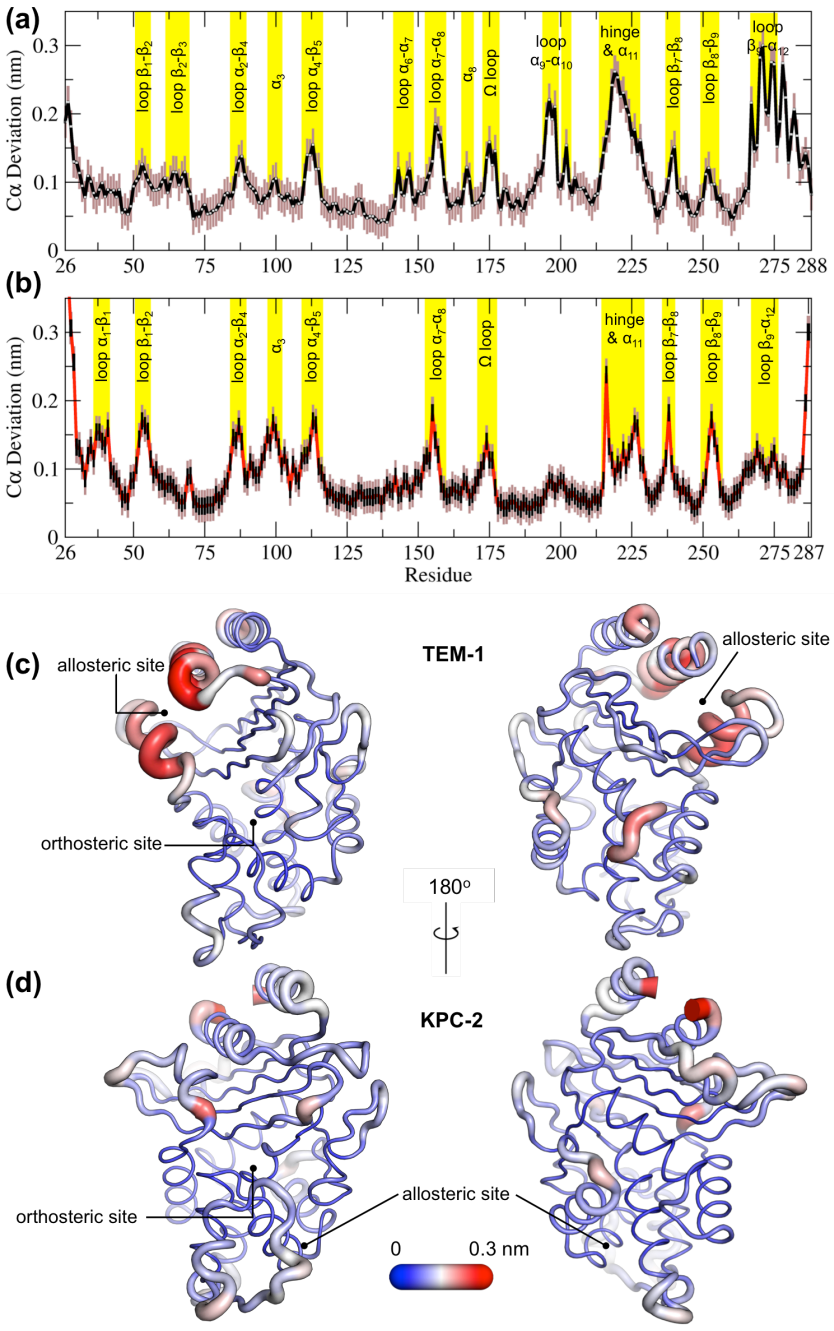

Figure 3. Average positional Cα deviations between the Apo_{EQ} and IB_{EQ} states of (a) TEM-1 and (b) KPC-2. Important structural motifs are highlighted and labeled on the plots. The brown vertical lines represent the standard deviation of the mean. The averaged Cα positional deviations mapped on the averaged Apo_{EQ} structures of (c) TEM-1 and (d) KPC-2, to visualize the largest relative displacements. The average deviation was determined from a combination of all 20 Apo_{EQ} and 20 IB_{EQ} trajectories. The thickness of the cartoon corresponds to the Cα deviation.

Figure 3–Figure supplement 1. Positional Cα Root Mean Square Fluctuation (RMSF) of TEM-1 Apo_{EQ}, TEM-1 IB_{EQ}, KPC-2 Apo_{EQ} and KPC-2 IB_{EQ} systems.

Figure 3–Figure supplement 2. Snapshot of the last frame from TEM-1 IB_{EQ} and KPC-2 IB_{EQ} replicate simulations.

Figure 3–Figure supplement 3. Average Cα deviation between the IB_{EQ} and Apo_{NE} calculated using the subtraction method for TEM-1 and KPC-2.

β4-α3 leading into α3 helix (residues 96-102) has the potential to deform the α3 helix-turn-α4 helix. The β4-α3 and α4-β5 loops form the basal pivot joint of the α3 and α4 helices and maintain the correct positioning of this helix-turn-helix at the periphery of the enzyme active site. The correct positioning of this loop is important as Trp105 lies on this loop. Mutagenesis studies have shown that a highly conserved aromatic amino acid at position 105 in class A β-lactamases (Tyr105 in TEM-1, Trp105 in KPC-2) is located at the perimeter of the active site and plays a crucial role in ligand recognition via favorable stacking interactions with the β-lactam ring (***Papp-Wallace et al., 2010b***; ***Doucet et al., 2004***). The aromatic side chain at position 105 coordinates the binding of substrates not only via stacking and edge-to-face interactions but by also adopting "flipped-in" or "flipped-out" conformations (***Galdadas et al., 2018***; ***Papp-Wallace et al., 2010b***,a). This has been proposed based on the conformations observed in the available crystal structures and confirmed by enhanced sampling molecular dynamics simulations (***Galdadas et al., 2018***; ***Ke et al., 2012***). Any perturbation that alters the conformation of α3-turn-α4 helix or deforms the α3-α4 pivot region would prevent α3 and α4 helices from correctly shaping the active site of the enzyme. This would result in the aromatic residue at 105 partially detaching from the edge of the active site and being unable to stabilize the incoming substrate as required for efficient catalysis. This explains the loss of β-lactam resistance in strains expressing KPC variants at positions 102 or 108, as established in the MIC experiments reported previously (***Galdadas et al., 2018***).

Signal propagation from the allosteric site

To study signal propagation from the two allosteric sites, we ran 800 short nonequilibrium (NE) simulations, with a total sampling time of 4 μs for each system. The nonequilibrium simulations were initiated from regular intervals of the equilibrated part of the long IB_{EQ} simulation, starting at the 50 ns time point (***Figure 2–Figure Supplement 1***). In each simulation, the ligand was removed from its binding site and the resulting system was further simulated for 5 ns. The response of the system to the perturbation was determined using the Kubo-Onsager approach developed by Ciccotti et al. (***Ciccotti and Ferrario, 2013***; ***Ciccotti et al., 1979***; ***Ciccotti and Ferrario, 2016***). In this approach, the time evolution of the conformational changes induced by ligand removal can be determined by comparing the Apo_{NE} and IB_{EQ} simulations at equivalent points in time. The subtraction method, applied to multiple pairs of trajectories, effetively removes noise arising from fluctuations of the systems and allows residues that are involved in signal propagation to be identified. The disappearance of the ligand from its binding site generates a temporary localized vacuum, against which there is an immediate structural and solvent response. As the simulation progresses, the cascading conformational changes in response to the perturbation (removal of ligand) show the route by which structural response is transmitted through the protein.

This approach has identified a general mechanism of signal propagation in nicotinic acetylcholine receptors, by analyzing their response to deletion of nicotine (***Oliveira et al., 2019b***). The difference in the position of Cα atoms is calculated between the short Apo_{NE} and IB_{EQ} simulations at specific time points. These differences are then averaged over all pairs of simulations to reveal the structural conformations associated with this response (Figure 4) and their statistical significance. The Cα coordinates of each residue in the Apo_{NE} were subtracted from the corresponding Cα atom coordinates of the IB_{EQ} simulation at specific points in time, namely 0.05, 0.5, 1, 3, and 5 ns. This resulted in a difference trajectory for each pair of simulations. The difference trajectories are averaged over the set of 800 simulations for each system. The low standard error calculated for the average between the Apo_{NE} and IB_{EQ} demonstrates the statistical significance of the results. Due to the short timescale (5 ns) of the nonequilibrium simulations, only small amplitude conformational changes will be observed.

In TEM-1, the allosteric site is sandwiched between the α11 and α12 helices. Adjacent to this binding site is the hinge region (residues 213-218), whose dynamics have previously been examined by NMR and shown to have low order parameters indicating high mobility (***Gobeil et al., 2019***; ***Savard and Gagné, 2006***). This is also the site of perturbation in the nonequilibrium simulations

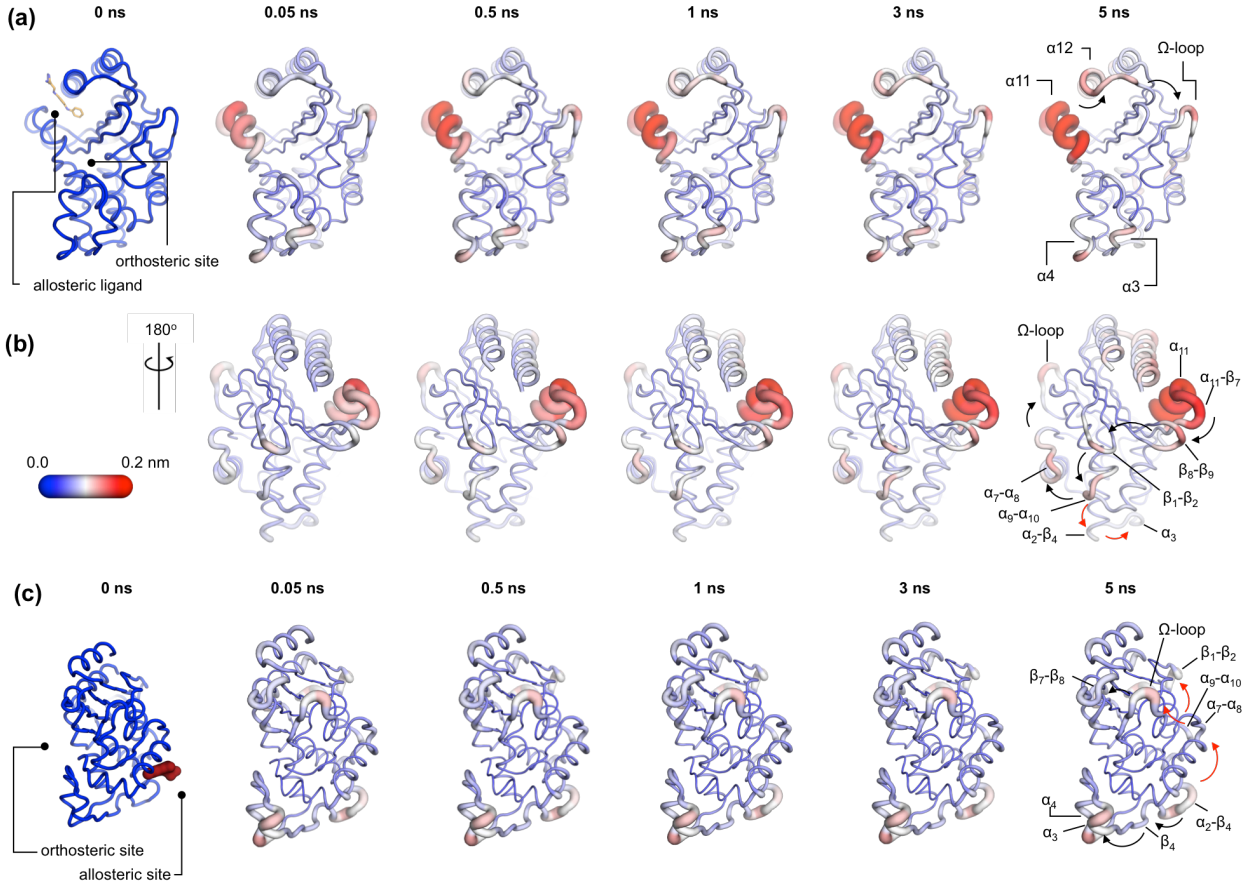

Figure 4. Communication pathways in (a, b) TEM-1 and (c) KPC-2. The average Cα deviations correspond to the average difference in the position of each Cα atom between all 800 pairs of IB_{EQ} and Apo_{NE} simulations at specific time points. The averaged Cα deviations are mapped on the average Apo_{EQ} structure. The arrows mark the direction of the propagation of the signal, caused by the perturbation (removal of the ligand). The red and the black arrows highlight different paths taken by the propagating signals (Also see movies ***Figure 4–video 1***, ***Figure 4–video 2***, ***Figure 4–video 3***).

Video supplements Signal propagation in TEM-1 and KPC-2 as a result of the perturbation (ligand removal) in the allosteric binding site. The disappearance of the ligand from its binding site generates a localized vacuum, against which there is an immediate structural response by the enzyme. As the simulation progresses, the cascading conformational changes in response to the perturbation (ligand removal) show the route by which structural response is transmitted through the protein.

Figure 4–video 1. Signal propagation in TEM-1 (front view).

Figure 4–video 2. Signal propagation in TEM-1 (back view).

Figure 4–video 3. Signal propagation in KPC-2.

and so the point of origin of the allosteric signal. Located on the loop between the distal end of the α11 helix and β7 is a highly conserved Trp229 residue. The indole ring of Trp229 is sandwiched between two other highly conserved residues, Pro226 and Pro251 present in loops α11-β7 and β8-β9 respectively. The π/aliphatic stacked arrangement of tryptophan-proline is a very tight interaction and is similar in geometry to that observed in complexes of proline-rich motif-binding families, including the EVH1 and GYF binding domains, with their peptide ligands (***Ball et al., 2005***; ***Freund et al., 1999***; ***Reinhard et al., 1996***; ***Zondlo, 2013***). The perturbation destabilizes this stacked arrangement resulting in an extension of an inherently highly mobile region. After 50 ps of simulation, the Cα deviations have propagated and can be observed in the loop between β1 and β2. Interestingly, the loops at the basal pivot of 3 and 4 also responded rapidly to ligand removal. These loops are ~33 Å away from the allosteric binding site and can affect the spatial position of the turn between helix α3 and α4. The α3-turn-α4 helix forms the boundary of the active site, and it is on this turn where the Tyr105 residue, important for substrate recognition is positioned. These results clearly demonstrate the coupling between the distal allosteric site and catalytically relevant regions of the enzyme. As the signal propagates within the protein, there is a gradual and cumulative increase in the Cα deviations in the aforementioned loops. In particular, the loop between the α9 and α10 helices, which is positioned just below the β1-β2 loop, displays high deviations and forms a focal point for the signal to bifurcate in two directions. First, major deviations are observed laterally towards loop α7-α8 and onwards into the Ω loop (***Figure 4***a,b). Second, more minor deviations move into the loop between α2-β4 and onwards into the basal pivot of α3-turn-α4 helix. There is another shorter route at the top of the enzyme that the signal can take to go from the allosteric binding site to the Ω loop, via the proximal end of α12 helix and across the loop between β9-α12 helix (***Figure 4***a,b).

In KPC-2, the allosteric pocket is shallower and lies between helices α2 and α7. Residues from three loops (α6-α7, α7-α8 and α2-β4) are in close proximity to this binding site. An additional loop, α9-α10, is linked to this binding site via the distal end of the α2 helix. The perturbation in this binding site results in enhanced mobility of the α2-β4 loop, which leads directly into β4 and onwards to the basal pivot of the α3 helix. The proximal end of the α3 helix and the distal end of the α4 helix, which forms the pivot point of the α3-turn-α4 structure, display high deviations (***Figure 4***c). The highly conserved aromatic amino acid, Trp105, is located on this turn. The distance between the allosteric binding site and the α3 helix is ~27 Å. Other major deviations are also observed in the Ω loop as the simulation progresses (***Figure 4***c). The Ω loop is directly linked to the allosteric binding site via loop α7-α8. Some minor deviations are also observed in the loop connecting β9 and the α12 helix.

In both TEM-1 and KPC-2, the removal of the ligand at the beginning of the nonequilibrium simulations does not result in large conformational changes. The subsequent Cα deviations trace the route of the propagating signals (***Figure 3–Figure Supplement 2***12). In TEM-1, α11 and the hinge region, loop β1-β2 and loop β8-β9 respond rapidly to the perturbation and display comparable RMSD values to the equilibrated simulations. Similarly, in KPC-2, only loops α2-β4 and α7-α8 respond rapidly to the perturbation. The other structural elements take longer to respond, and their conformational rearrangements are not fully sampled in the Apo_{NE} simulations. It is worth emphasizing that while the short nonequilibrium simulation can be an excellent tool to study an immediate structural response towards a perturbation, the timescale of nonequilibrium MD does not represent a real timescale and thus should not be compared directly with equilibrium simulations. Nevertheless, nonequilibrium MD can identify the sequence of events and pathways involved.

The perturbations of the two enzymes here are different but show some striking common features. In both TEM-1 and KPC-2 systems, even though the point of origin of perturbation (i.e. allosteric site) is different, the signal leads to common endpoints at the pivot of α3-turn-α4 helix and in the Ω loop. Thus, simulations of two different class A β-lactamases, starting from two distinct allosteric sites, identify a common mechanism by which catalytic activity may be disrupted by conformational changes close to the active site. The results from the nonequilibrium simulations also

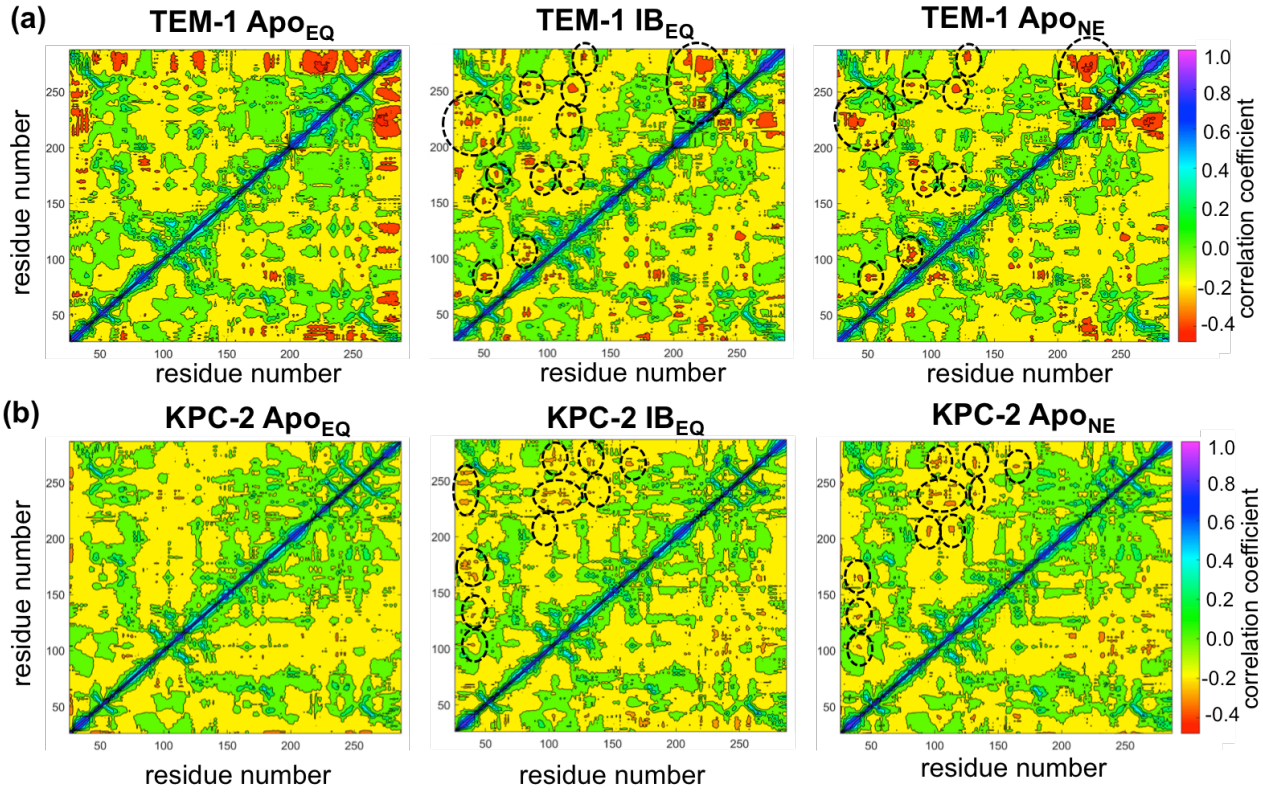

Figure 5. Dynamic Cross-Correlation Maps (DCCMs) computed for (a) TEM-1 and (b) KPC-2 Apo equilibrium (Apo$_{EQ}$), inhibitor-bound equilibrium (IB$_{EQ}$) and Apo nonequilibrium (Apo$_{NE}$) trajectories. The DCCMs for equilibrium trajectories were calculated as an average of 20 replica simulations, while the Apo nonequilibrium DCCM indicates an averaged DCCM from an ensemble of 40 short (5 ns) MD trajectories. Green regions indicate no correlation; yellow indicates moderate negative correlation while orange and red indicate significant negative correlations, while blue regions indicate positive correlations. In TEM-1 Apo$_{NE}$, regions showing significant changes from Apo$_{EQ}$ and IB$_{EQ}$ bound simulations have been marked by black dashed ellipses.

Figure 5–Figure supplement 1. TEM-1 averaged DCCM computed from all nonequilibrium trajectories.

Figure 5–Figure supplement 2. Selected DCCMs computed for individual 5 ns nonequilibrium MD trajectories of KPC-2.

correlate well with experimental data, which suggest that the Ω loop plays a critical role in ligand binding by altering the conformation of Glu166 and Asn170 which are involved in both acylation and deacylation reactions (***Chudyk et al., 2014***; ***Pan et al., 2017***; ***Brown et al., 2009***; ***Fritz et al., 2018***; ***Banerjee et al., 1998***).

Dynamic cross-correlation analysis of surface loops

Dynamical cross-correlation analysis provides information about the pathways of signal propagation and also some insights into the timescales of allosteric communication in TEM-1 and KPC-2 β-lactamases. Dynamic cross-correlation maps (DCCM) have been previously used to identify networks of coupled residues in several enzymes (***Agarwal et al., 2004***; ***Hester et al., 2019***; ***Agarwal et al., 2012***).

Using a similar approach, DCCMs were calculated for the Apo$_{EQ}$ and IB$_{EQ}$ simulations and also for the Apo$_{NE}$ nonequilibrium simulations (***Figure 5***). In these figures, the green regions represent no to slightly positive correlations, while yellow regions represent moderate negative correlations. Negative correlations imply residues moving towards or away from each other in correlated fashion (such as shown by fluctuating hydrogen bonds); for large regions this represents global conformational fluctuations (also referred to as breathing motions) (***Agarwal et al., 2004***). The results depicted in ***Figure 5***a indicate that in the case of TEM-1 Apo$_{EQ}$ (***Figure 5***a, left), β11 helix shows high negative correlation with β12 terminal helix. This represents the lid motion of β12 helix, which

moves to shut the empty, hydrophobic, allosteric binding site in the TEM-1 Apo_{EQ} structure (see above). This motion is, however, not observed in the ligand bound TEM-1 IB_{EQ} simulations. The TEM-1 IB_{EQ} system shows a substantial increase in correlations, representing changes in the dynamical communications due to the presence of the allosteric ligand (***Figure 5***a, middle). The binding of the ligand changes the overall global conformational fluctuations of TEM-1, as represented by the increase in yellow regions in the DCCMs. Furthermore, a number of negative correlations (encircled red regions in DCCMs) also increase in other regions of the protein on ligand binding. The DCCM collectively computed from all nonequilibrium trajectories for TEM-1 (***Figure 5***a, right, ***Figure 5–Figure Supplement 1***) also shows a further increase in the areas of negative correlations (encircled). Interestingly, DCCM also identifies the pathway of allosteric communication (***Figure 5–Figure Supplement 1***), with notable correlations between the regions β1-β2:α2-β4, α3-α4:α2-β4, β4-α3:α7-α8, β3-α2:Ω, α9-α10:β1-β2, β3-α2:β8-β9, α5-α6:α12, hinge-α11:α1-β1, β8-β9:α4-β5, β7:α12 and α11:α12. These results indicate that the presence of ligand in TEM-1 increases the dynamic communication between regions that are independent in the Apo_{EQ} simulations. This is particularly evident in the nonequilibrium trajectories that show the largest changes from the case of Apo_{EQ} TEM-1, identifying changes in correlation as the system adjusts to the absence of the ligand.

KPC-2 shows even more interesting behavior (***Figure 5***b). Simulations of Apo_{EQ} KPC-2 show overall more correlated regions than TEM-1 Apo_{EQ} system (as indicated by the more extensive yellow regions in the DCCM), with further increases in the presence of the inhibitor (indicated by a number of orange regions). However, the DCCM collectively computed from all nonequilibrium trajectories for KPC-2 shows a reduction in regions of cross-correlations; a contrast from the case of TEM-1. To obtain a better understanding, the DCCMs from individual 5 ns nonequilibrium trajectories were also computed and analyzed. These reveal interesting trends as depicted in ***Figure 5–Figure Supplement 2***. For most nonequilibrium trajectories, the maps are similar with a decrease in dynamic correlations, however, for several trajectories (shown in ***Figure 5–Figure Supplement 2***) the maps indicate a significant increase in the correlations. The DCCMs computed from individual trajectories show behavior similar to averaged nonequilibrium trajectories in TEM-1 with a number of regions showing high negative correlations (as highlighted by wide-spread presence of small red regions in the DCCMs). Overall, these results indicate that the perturbation in KPC-2 generates a dynamical response that is much faster than that observed in TEM-1. A plausible explanation for the faster response in KPC-2 is that the more solvent-exposed ligand binding site is surrounded by dynamic surface loops that respond to the perturbation more quickly than the allosteric binding site in TEM-1, which is buried in the hydrophobic core of the protein. This is consistent with the experimental observations that motions can occur on different timescales and can vary greatly between different β-lactamases (***Gobeil et al., 2019***).

Relating enzyme dynamics to positions of substitution in TEM-1 and KPC-2 clinical variants

A number of clinical variants that extend hydrolytic activity to encompass additional β-lactams such as oxyiminocephalosporins, and/or enhance enzyme stability, have been identified for both the TEM-1 and KPC-2 β-lactamase enzymes (***Palzkill, 2018***; ***Clark et al., 2016***; ***Naas et al., 2017***). Some of these have been crystallized and their protein structure deposited in the PDB. While many of these amino acid substitutions (for example TEM-1 mutations at residues Glu104 in the α3-turn-α4, Arg164 on the Ω-loop and Ala237, Gly238 and Glu240 on the β7 strand) directly affect important structural features such as the active site or the Ω loop, some are of uncertain structural significance. Even when enzyme structures are known, the connections between the positions of clinical variants, protein structure and their functional implications are often not clear. There is particular uncertainty and interest in the effects of mutations more distant from the active site.

To assess how many of these clinically relevant substitutions lie on the allosteric communication pathway, their spatial positions were identified and mapped onto the 3D structures of TEM-1 and KPC-2. The site of the mutation was plotted as a sphere on its unique Cα position on the struc-

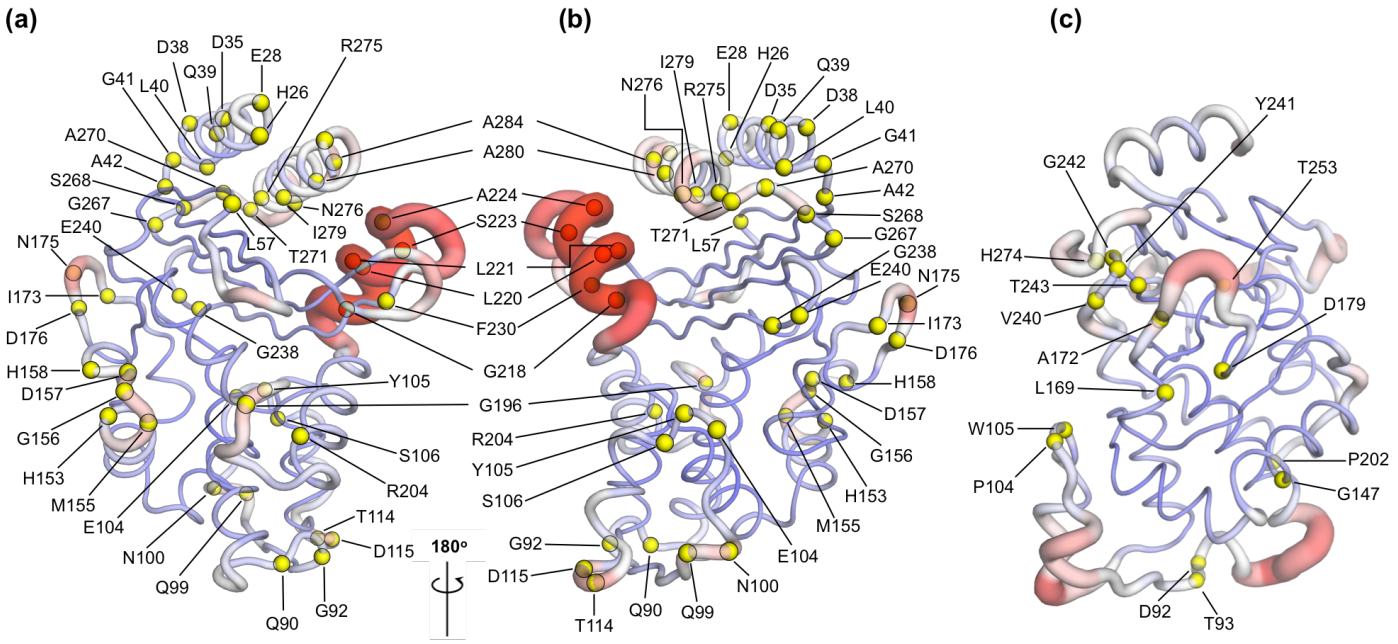

Figure 6. Variant positions in (a, b) TEM-1 and (c) KPC-2 mapped on the averaged Apo_{EQ} structures, also showing allosteric communication pathways (See ***Figure 4***) identified by nonequilibrium simulations. The position of the variant is shown as yellow spheres centered at the corresponding Cα. Only the sites of mutations that lie on the allosteric communication pathways have been annotated. The color scheme and cartoon thickness of the rendered structures represents a snapshot of average Cα deviation between IB_{EQ} and Apo_{NE}. Many of these clinically important variant positions lie on the allosteric communication pathway: 45 of the 90 for TEM-1, 15 out of the 25 for KPC-2 single point variants lie on the pathways. This suggests that these variations affect the allosteric behavior of the enzymes.

Figure 6–Figure supplement 1. Spatial position of M182 and A184 on TEM-1.

ture (***Figure 6***), which was rendered to represent the allosteric communication pathways shown in ***Figure 4***.

For TEM-1, 45 of the 90, and for KPC-2 15 out of the 25, amino acid positions known to vary in clinical isolates could be mapped on the allosteric communication pathway. Notably, in TEM-1, residues such as Gly92 preceding α4, His153 at the end of α7, and Ala224 preceding α11; have all been associated with ESBL and/or inhibitor resistant phenotypes identified in the clinic (***Palzkill, 2018***). Residues such as M182 and A184, which precede α9 and are not on the communication pathway per se; are however surrounded on all sides by loops that are involved in the communication network (***Figure 6–Figure Supplement 1***). For KPC enzymes, for which less information is available, characterized variants that have emerged in the clinic differ mostly in activity towards ceftazidime 58 and feature substitutions at positions (104, 240, 274) closer to the active site. As more sequences emerge and their phenotypic consequences are described (***Tooke et al., 2021***), however, it will then be of interest to establish the properties of KPC variants featuring substitutions at positions (e.g. 92, 93), which lie along the communication pathways described here. We propose that some of these variants differ in allosteric properties, and further, that these differences relate to variances in their clinically relevant spectrum of activity. If our hypothesis is correct, 50% or more of known clinically important variants in these two enzymes may differ in their allosteric behavior, indicating that this is a fundamentally important property in determining their spectrum of catalytic activity. The relationship between sequence (especially substitutions remote from the active site), protein dynamics, spectrum of activity, catalytic turnover and allosteric behavior, will be an important future direction in understanding antimicrobial resistance due to β-lactamase enzymes (***Tooke et al., 2021***).

Discussion

Here, we have identified structural communication between two allosteric binding sites and structural elements, close to the active site, that control enzyme specificity and activity in two distinct, clinically important, class A β-lactamases. The extensive equilibrium MD simulations, with and without ligands, reveal ligand-induced conformational changes, while nonequilibrium MD simulations show that changes at allosteric sites are transmitted to the active site, and identify the structural pathways involved. These nonequilibrium simulations identify the initial stages of the dynamic rearrangement of secondary structural elements and identified the signal propagation routes (with demonstration of its statistical significance). These two complementary approaches together facilitate understanding of how information flows from one part of the protein structure to another.

The equilibrium simulations (of ligand-bound and Apo enzymes) show that the structural effects of ligand binding to allosteric sites are not restricted to the local binding pocket. Class A β-lactamases are rigid enzymes (***Gobeil et al., 2019***) that do not undergo large-scale conformational changes; the observed structural rearrangements (caused by ligand removal) are dominated by localized changes in the conformation of loops. Such ligand-induced structural changes are observed in the loops surrounding the active sites including the hinge region, the Ω loop and the α3-turn-α4 helix, positioned as far as ~33 Å from the allosteric ligand binding site. In both enzymes, the observed flexible motions lead to an enlargement of the active site, with the potential consequences for the orientation of either mechanistically important regions of the protein or of bound ligand, and, consequently, enzyme activity.

The nonequilibrium simulations, using an emerging technique, identify the structural rearrangements arising as a result of a perturbation (ligand removal) and demonstrate communication between the allosteric site and the active site. The ordering of these conformational changes shows the initial steps of communication between secondary structure elements. This structural relay constitutes a pathway that enables effective signal propagation within the enzymes. In TEM-1, the conformational changes initiated at the allosteric site (which is situated between helices α11-α12) proceed via the β1-β2 loop to the α9-α10 loop. From this point, the signal bifurcates towards the Ω loop via the α7-α8 loop or towards the α3-α4 pivot via the α2-β4 loop. In KPC-2, the perturbation caused by ligand unbinding between the α2 and α7 helices results in conformational changes in loop α2-β4, leading to β4 and onwards to the pivot of the α3-turn-α4 helix. These conformational changes are relayed to the Ω loop via the α7-α8 loops. In addition, the signal can also take another route from the α7-α8 loop towards the β9-α12 loop, which lies adjacent to the hinge region. It is worth emphasizing that the TEM-1 and KPC-2 systems display a striking resemblance in that the flow of information is towards a common endpoint, despite the two different points of origin. Thus, even though the propagation pathway taken is different, in each case, the signals accumulate to have a structural impact on the conformation of the Ω loop and the α3-turn-α4 helix. These results demonstrate communication between allosteric ligand binding sites and the active sites of the enzymes, which could be exploited in alternative strategies for inhibitor development.

All class A β-lactamase enzymes share conserved structural architecture (***Philippon et al., 2016***; ***Galdadas et al., 2018***). Mutational studies and the location of sites of substitutions in clinical variants suggest the importance to activity of the hinge region, Ω loop and α3-turn-α4 helix, including the spatial position of the conserved aromatic residue at 105 (or the analogous position in other class A β-lactamases) (***Palzkill, 2018***; ***Philippon et al., 2016***; ***Banerjee et al., 1998***; ***Papp-Wallace et al., 2010b***). Perturbations around these sites, as identified in the simulations here, may constitute a general mechanism by which a conformational signal transmitted from an allosteric site is relayed via cooperative coupling of loop dynamics to affect catalytic activity. Exploitation of such signaling networks may constitute a novel strategy for the development of new types of inhibitors for these key determinants of bacterial antibiotic resistance.

Methods and Materials

Protein structure preparation

To study allosteric modulation of class A β-lactamases, we started by identifying crystal structures of TEM-1 and KPC-2 β-lactamases with allosteric ligands bound. From the ~80 structures present in the Protein Data Bank (PDB), there are only two crystal structures of class A β-lactamases that have a ligand bound in an allosteric pocket. For TEM-1, the 1.45 Å crystal structure in complex with FTA [3-(4-phenylamino-phenylamino)-2-(1h-tetrazol5-yl)-acrylonitrile] was chosen as the starting structure (PDB id: 1PZP) for this work ***Horn and Shoichet*** (***2004***). In this structure, the inhibitor binds between helices α11 and α12 (***Figure 1***a), in a site ~16 Å away from the active site Ser70. Two unstructured residues from the C-terminal end (His289, Trp290) were removed from the crystal structure. For KPC-2, the 1.35 Å crystal structure in complex with a coumarin phosphonate analogue, GTV [(5,7-dimethyl-2-oxo-2h-1-benzopyran-4-yl)methyl]phosphonic acid], was chosen as the starting structure (PDB id: 6D18) (***Pemberton et al., 2019***). GTV binds in three sites on KPC-2 (***Figure 1***b): the first is in the active site (orthosteric ligand); the second site is adjacent to helix α6 (allosteric ligand 1); and the third (allosteric ligand 2) is on the distal end of the enzyme, ~16 Å from the active site Ser70 in between helices α2 and α7. The orthosteric and allosteric ligand1 (Figure 1b) were discarded because of their direct proximity to the active site and replaced by water. Three unstructured residues from the N-terminal end (His23, Met24, Leu25) and seven from the C-terminal end (Leu288-Gly294) were removed from the starting structure to avoid any simulation artifacts arising as a result of terminal fraying during simulations.

The protonation states of the amino acid side chains were determined at pH 7.0, using the *ProteinPrepare* functionality as implemented in the High-Throughput Molecular Dynamics (HTMD) framework (***Martínez, 2015***; ***Doerr et al., 2016***). Charges were assigned on the basis of their local environment, via optimization of the hydrogen-bonding network of the protonated structure (***Martínez, 2015***).

Parameters for the ligands were generated using the Antechamber tool (***Case et al., 2005***). The geometry was optimized at the B3LYP/6-31G(d) level and RESP charges were fitted using electrostatic potential obtained at the HF/6-31G(d) level. The necessary nonbonded parameters for the dynamics of the ligands were adopted from GAFF2 (***Wang et al., 2004***).

MD simulations details

All complexes were set up using tleap, as implemented in the Amber MD package.8 The Amber ff14SB forcefield (***Maier et al., 2015***) was used for the protein. In total, four complexes were set up, including an allosteric inhibitor-bound (IB) and an Apo (no ligand) system for both TEM-1 and KPC-2 β-lactamases. The Apo system was generated by removing the inhibitor from the allosteric binding site. In all simulated complexes, there is no ligand bound to the orthosteric site. Each complex was solvated using TIP3P water in a cubic box, whose edge was set to at least 10 Å from the closest solute atom ***Mark and Nilsson*** (***2001***). The systems were neutralized using K^+ and Cl^- counter ions. The simulation protocol was identical for each system. The systems were minimized and relaxed under NPT conditions for 5 ns at 1 atm. The temperature was increased to 300 K using a timestep of 4 fs, rigid bonds and a cutoff of 9 Å and particle mesh Ewald summations switched on for long-range electrostatics (***Essmann et al., 1995***). During the equilibration step, the protein's backbone and the ligand atoms were restrained by a spring constant set at 1 kcal mol^{-1} $Å^{-2}$, while the ions and solvent were free to move. The production simulations were run in the NVT ensemble using a Langevin thermostat with a damping constant of 0.1 ps and hydrogen mass repartitioning scheme to achieve a time step of 4 fs (***Feenstra et al., 1999***). The final production step was run without any restraints. All simulations were run using the ACEMD molecular dynamics engine as implemented in the HTMD framework (***Doerr et al., 2016***). Visualization of the simulations was done using the VMD package (***Humphrey et al., 1996***).

Equilibrium simulations

In order to sufficiently sample the conformational space, 20 replicate simulations of 250 ns each were performed for each system. This resulted in a total sampling time of 5 μs for each system. The initial velocities of the atoms of each replica were randomized. We describe this set of runs in this study as equilibrium simulations (Apo_{EQ}/IB_{EQ}).

Nonequilibrium simulations

To investigate rapid conformational changes and study signal propagation within the proteins, we carried out 800 short nonequilibrium MD simulations for each system. Such nonequilibrium simulations have been applied successfully to study interdomain communication in receptors and other systems like ABC transporters (***Abreu et al., 2020***; ***Damas et al., 2011***; ***Oliveira et al., 2019b***,a, ***2005***). We used the Kubo-Onsager approach (***Ciccotti and Ferrario, 2013***, ***2016***; ***Ciccotti et al., 1979***) to extract the conformational response of the proteins to ligand removal. In this approach, the response of a system to a perturbation is computed by calculating the difference in the evolution of the simulations with and without the perturbation. Subtracting the perturbed and unperturbed pairs of simulations at a given time, and averaging the results over multiple replicates, allows not only for the identification of the events associated with signal propagation but also determines the statistical significance of the observations. When the two sets of simulations (with and without a perturbation) are correlated, the subtraction technique permits the cancellation of noise arising from random intrinsic fluctuations of the system thus allowing the identification of the response to the perturbation in a statistically significant way (***Ciccotti et al., 1979***). In our systems, the perturbation was generated by (instantaneously) removing the ligand from the allosteric pocket. It is important to emphasize that the annihilation of the ligand in this way does not represent the physical process of unbinding. The objective is to rapidly elicit response and force signal propagation within the protein, as the conformation adjusts to the removal of the ligand. Such a response allows for the identification of the initial signals that are sent out as conformational changes associated with the signal propagating from the allosteric binding pocket. The structural rearrangements in the communication pathways revealed by nonequilibrium simulations are likely to be involved in response to the physical process of binding and unbinding of ligands in the allosteric pockets.

A graphical representation of the procedure that was followed to setup the nonequilibrium simulations is given in ***Figure 2–Figure Supplement 1***. The starting conformation for the short nonequilibrium simulations (Apo_{NE}) was extracted from the equilibrated part of the 250 ns equilibrium simulations (50-250 ns). Specifically, conformations were taken every 5 ns, the ligand was removed from the allosteric pocket and the resulting Apo_{NE} system was run for another 5 ns (***Figure 2–Figure Supplement 1***). 40 short, nonequilibrium simulations were run for each replicate. In total 800 simulations were run for each system. The simulation conditions of the nonequilibrium simulations were identical to those in the equilibrium simulations.

For each pair of unperturbed IB_{EQ} and perturbed Apo_{NE} simulations, the difference in positions for each Cα was determined at equivalent points in time, namely at 0, 0.05, 0.5, 1, 3 and 5 ns. Calculating the differences in the positions of Cα identifies conformational rearrangements, while reducing the noise coming from side chain fluctuations. The Cα deviation values at each time point were averaged over all 800 simulations. To assess the statistical significance of the conformational response over hundreds of simulations performed, the standard deviation (SD) and standard error (SE) of the mean (95% confidence interval) were determined. Overall, low SD and SE values observed for all the regions of interest (as illustrated for e.g. in Figure 3) demonstrate the statistical significance of the results.

Analysis details

The analysis was carried out using GROMACS tools (***Abraham et al., 2015***), MDLovofit (***Martínez, 2015***) and in-house scripts (***Oliveira et al., 2019b***). All systems were considered equilibrated after 50 ns. The dynamic cross-correlations for Cα-Cα were calculated using cpptraj analysis program

(***Roe and Cheatham, 2013***). The results were plotted using in-house scripts and visualized using MATLAB (www.mathworks.com).

An independent-samples Student's t-test was used to compare the Apo_{EQ} and IB_{EQ} RMSFs and to assess the significance of the differences observed (***Oliveira et al., 2019b***; ***Roy and Laughton, 2010***). The sample size used for the t-test was the 20 RMSF profiles of the Apo_{EQ} and IB_{EQ} independent simulations. The assumption used for the t-test was that the samples from the two states were independent, the dependent variable was normally distributed and the variances of the dependent variable were equal.

The figures were made using PyMol (www.schrodinger.com), VMD (***Humphrey et al., 1996***), ChimeraX (***Goddard et al., 2018***), Protein Imager (3dproteinimaging.com) (***Tomasello et al., 2020***) and Molsoft ICM-Pro package (www.molsoft.com).

Acknowledgments

IG is funded by Astra Zeneca-EPSRC case studentship awarded to FLG and SH. PKA acknowledges a grant from the National Institute of General Medical Sciences of the National Institutes of Health USA under award number GM105978. SH and RB acknowledge a grant from the National Institutes of Health USA under the award number RO1AI063517. AJM and ASF thank EPSRC for support (grant numbers EP/M022609/1 and EP/N024117/1) and also thank BrisSynBio, a BBSRC/EPSRC Synthetic Biology Research Centre (Grant Number: BB/L01386X/1) for funding. AJM, JS and CLT also thank MRC for support (grant number MR/T016035/1). RAB is supported by the National Institute of Allergy and Infectious Diseases of the National Institutes of Health (NIH) under Award Numbers R01AI100560, R01AI063517, and R01AI072219 and in part by funds and/or facilities provided by the Cleveland Department of Veterans Affairs, Award Number 1I01BX001974 from the Biomedical Laboratory Research Development Service of the VA Office of Research and Development, and the Geriatric Research Education and Clinical Center VISN 10. The content is solely the responsibility of the authors and does not necessarily represent the official views of the NIH or the Department of Veterans Affairs.

References

Abraham MJ, Murtola T, Schulz R, Páll S, Smith JC, Hess B, Lindahl E. GROMACS: High performance molecular simulations through multi-level parallelism from laptops to supercomputers. SoftwareX. 2015 Sep; 1-2:19–25. https://linkinghub.elsevier.com/retrieve/pii/S2352711015000059, doi: 10.1016/j.softx.2015.06.001.

Abreu B, Lopes EF, Oliveira ASF, Soares CM. F508del disturbs the dynamics of the nucleotide binding domains of CFTR before and after ATP hydrolysis. Proteins: Structure, Function, and Bioinformatics. 2020 Jan; 88(1):113–126. https://onlinelibrary.wiley.com/doi/abs/10.1002/prot.25776, doi: 10.1002/prot.25776.

Agarwal PK. A Biophysical Perspective on Enzyme Catalysis. Biochemistry. 2019 Feb; 58(6):438–449. https://pubs.acs.org/doi/10.1021/acs.biochem.8b01004, doi: 10.1021/acs.biochem.8b01004.

Agarwal PK, Geist A, Gorin A. Protein Dynamics and Enzymatic Catalysis: Investigating the PeptidylProlyl CisTrans Isomerization Activity of Cyclophilin A †. Biochemistry. 2004 Aug; 43(33):10605–10618. https://pubs.acs.org/doi/10.1021/bi0495228, doi: 10.1021/bi0495228.

Agarwal PK, Schultz C, Kalivretenos A, Ghosh B, Broedel SE. Engineering a Hyper-catalytic Enzyme by Photoactivated Conformation Modulation. The Journal of Physical Chemistry Letters. 2012 May; 3(9):1142–1146. https://pubs.acs.org/doi/10.1021/jz201675m, doi: 10.1021/jz201675m.

Ambler R. The structure of β-lactamases. Philosophical Transactions of the Royal Society of London B, Biological Sciences. 1980 May; 289(1036):321–331. https://royalsocietypublishing.org/doi/10.1098/rstb.1980.0049, doi: 10.1098/rstb.1980.0049.

on Antimicrobial Resistance ICG. No Time To Wait: Securing the Future From Drug-Resistant Infections. World Health Organization; 2019.

Ball LJ, Kühne R, Schneider-Mergener J, Oschkinat H. Recognition of Proline-Rich Motifs by Protein-Protein-Interaction Domains. Angewandte Chemie International Edition. 2005 May; 44(19):2852–2869. http://doi.wiley.com/10.1002/anie.200400618, doi: 10.1002/anie.200400618.

650 **Banerjee S**, Pieper U, Kapadia G, Pannell LK, Herzberg O. Role of the Ω-Loop in the Activity, Substrate Specificity,
651 and Structure of Class A β-Lactamase. Biochemistry. 1998 Mar; 37(10):3286–3296. https://pubs.acs.org/doi/
652 10.1021/bi972127f, doi: 10.1021/bi972127f.

653 **Bonomo RA**. β-Lactamases: A Focus on Current Challenges. Cold Spring Harbor Perspectives in Medicine.
654 2017 Jan; 7(1):a025239. http://perspectivesinmedicine.cshlp.org/lookup/doi/10.1101/cshperspect.a025239, doi:
655 10.1101/cshperspect.a025239.

656 **Bowman GR**, Bolin ER, Hart KM, Maguire BC, Marqusee S. Discovery of multiple hidden allosteric
657 sites by combining Markov state models and experiments. Proceedings of the National Academy of
658 Sciences. 2015 Mar; 112(9):2734–2739. http://www.pnas.org/lookup/doi/10.1073/pnas.1417811112, doi:
659 10.1073/pnas.1417811112.

660 **Brown NG**, Shanker S, Prasad BVV, Palzkill T. Structural and Biochemical Evidence That a TEM-1 β-
661 Lactamase N170G Active Site Mutant Acts via Substrate-assisted Catalysis. Journal of Biological Chem-
662 istry. 2009 Nov; 284(48):33703–33712. http://www.jbc.org/lookup/doi/10.1074/jbc.M109.053819, doi:
663 10.1074/jbc.M109.053819.

664 **Bunzel HA**, Anderson JLR, Hilvert D, Arcus VL, van der Kamp MW, Mulholland AJ. Evolution of dynamical net-
665 works enhances catalysis in a designer enzyme. bioRxiv. 2020; https://www.biorxiv.org/content/early/2020/
666 08/23/2020.08.21.260885, doi: 10.1101/2020.08.21.260885.

667 **Bunzel HA**, Anderson JLR, Mulholland AJ. Designing better enzymes: Insights from directed evolution. Cur-
668 rent Opinion in Structural Biology. 2021; 67:212–218. https://www.sciencedirect.com/science/article/pii/
669 S0959440X21000075, doi: https://doi.org/10.1016/j.sbi.2020.12.015.

670 **Bush K**, Bradford PA. β-Lactams and β-Lactamase Inhibitors: An Overview. Cold Spring Harbor Perspec-
671 tives in Medicine. 2016 Jan; 6(8):a025247. http://perspectivesinmedicine.cshlp.org/content/6/8/a025247, doi:
672 10.1101/cshperspect.a025247, publisher: Cold Spring Harbor Laboratory Press.

673 **Bush K**, Jacoby GA. Updated functional classification of beta-lactamases. Antimicrobial Agents and Chemother-
674 apy. 2010 Mar; 54(3):969–976. doi: 10.1128/AAC.01009-09.

675 **Bush K**, Page MGP. What we may expect from novel antibacterial agents in the pipeline with respect to re-
676 sistance and pharmacodynamic principles. Journal of Pharmacokinetics and Pharmacodynamics. 2017 Apr;
677 44(2):113–132. https://doi.org/10.1007/s10928-017-9506-4, doi: 10.1007/s10928-017-9506-4.

678 **Case DA**, Cheatham TE, Darden T, Gohlke H, Luo R, Merz KM, Onufriev A, Simmerling C, Wang B, Woods RJ. The
679 Amber biomolecular simulation programs. Journal of Computational Chemistry. 2005 Dec; 26(16):1668–1688.
680 http://doi.wiley.com/10.1002/jcc.20290, doi: 10.1002/jcc.20290.

681 **Centers for Disease Control and Prevention (U S)**. Antibiotic resistance threats in the United States, 2019.
682 Centers for Disease Control and Prevention (U.S.); 2019.

683 **Chudyk EI**, Limb MAL, Jones C, Spencer J, van der Kamp MW, Mulholland AJ. QM/MM simulations as an assay
684 for carbapenemase activity in class A β-lactamases. Chem Commun. 2014; 50(94):14736–14739. http://xlink.
685 rsc.org/?DOI=C4CC06495J, doi: 10.1039/C4CC06495J.

686 **Ciccotti G**, Jacucci G, McDonald IR. Thought-experiments by molecular dynamics. Journal of Statistical Physics.
687 1979 Jul; 21(1):1–22. http://link.springer.com/10.1007/BF01011477, doi: 10.1007/BF01011477.

688 **Ciccotti G**, Ferrario M. Dynamical Non-Equilibrium Molecular Dynamics. Entropy. 2013 Dec; 16(1):233–257.
689 http://www.mdpi.com/1099-4300/16/1/233, doi: 10.3390/e16010233.

690 **Ciccotti G**, Ferrario M. Non-equilibrium by molecular dynamics: a dynamical approach. Molecular Simula-
691 tion. 2016 Nov; 42(16):1385–1400. https://www.tandfonline.com/doi/full/10.1080/08927022.2015.1121543, doi:
692 10.1080/08927022.2015.1121543.

693 **Clark K**, Karsch-Mizrachi I, Lipman DJ, Ostell J, Sayers EW. GenBank. Nucleic Acids Research.
694 2016 Jan; 44(D1):D67–D72. https://academic.oup.com/nar/article-lookup/doi/10.1093/nar/gkv1276, doi:
695 10.1093/nar/gkv1276.

696 **Damas JM**, Oliveira ASF, Baptista AM, Soares CM. Structural consequences of ATP hydrolysis on the ABC
697 transporter NBD dimer: Molecular dynamics studies of HlyB. Protein Science. 2011 Jul; 20(7):1220–1230.
698 http://doi.wiley.com/10.1002/pro.650, doi: 10.1002/pro.650.

699 **Doerr S**, Harvey MJ, Noé F, De Fabritiis G. HTMD: High-Throughput Molecular Dynamics for Molecular Discovery.
700 Journal of Chemical Theory and Computation. 2016 Apr; 12(4):1845–1852. https://pubs.acs.org/doi/10.1021/
701 acs.jctc.6b00049, doi: 10.1021/acs.jctc.6b00049.

702 **Doucet N**, De Wals PY, Pelletier JN. Site-saturation Mutagenesis of Tyr-105 Reveals Its Importance
703 in Substrate Stabilization and Discrimination in TEM-1 β-Lactamase. Journal of Biological Chem-
704 istry. 2004 Oct; 279(44):46295–46303. http://www.jbc.org/lookup/doi/10.1074/jbc.M407606200, doi:
705 10.1074/jbc.M407606200.

706 **Drawz SM**, Bonomo RA. Three Decades of β-Lactamase Inhibitors. Clinical Microbiology Reviews. 2010 Jan;
707 23(1):160–201. https://CMR.asm.org/content/23/1/160, doi: 10.1128/CMR.00037-09.

708 **Escobar WA**, Tan AK, Lewis ER, Fink AL. Site-Directed Mutagenesis of Glutamate-166 in .beta.-Lactamase Leads
709 to a Branched Path Mechanism. Biochemistry. 1994 Jun; 33(24):7619–7626. https://pubs.acs.org/doi/abs/10.
710 1021/bi00190a015, doi: 10.1021/bi00190a015.

711 **Essmann U**, Perera L, Berkowitz ML, Darden T, Lee H, Pedersen LG. A smooth particle mesh Ewald method.
712 The Journal of Chemical Physics. 1995 Nov; 103(19):8577–8593. http://aip.scitation.org/doi/10.1063/1.470117,
713 doi: 10.1063/1.470117.

714 **Feenstra KA**, Hess B, Berendsen H. Improving efficiency of large time-scale molecular dynamics simulations
715 of hydrogen-rich systems. Journal of Computational Chemistry. 1999; 20:786–798.

716 **Fisette O**, Gagné S, Lagüe P. Molecular Dynamics of Class A β-lactamases—Effects of Substrate Binding. Bio-
717 physical Journal. 2012 Oct; 103(8):1790–1801. https://linkinghub.elsevier.com/retrieve/pii/S0006349512010211,
718 doi: 10.1016/j.bpj.2012.09.009.

719 **Fisher J**, Mobashery S. Three Decades of the Class A beta-Lactamase Acyl-Enzyme. Current Protein & Peptide
720 Science. 2009 Oct; 10(5):401–407. http://www.eurekaselect.com/openurl/content.php?genre=article&issn=
721 1389-2037&volume=10&issue=5&spage=401, doi: 10.2174/138920309789351967.

722 **Freund C**, Wagner G, Dötsch V, Nishizawa K, Reinherz EL. The GYF domain is a novel structural fold that is
723 involved in lymphoid signaling through proline-rich sequences. Nature Structural Biology. 1999 Jul; 6(7):656–
724 660. http://www.nature.com/doifinder/10.1038/10712, doi: 10.1038/10712.

725 **Fritz RA**, Alzate-Morales JH, Spencer J, Mulholland AJ, van der Kamp MW. Multiscale Simulations of Clavu-
726 lanate Inhibition Identify the Reactive Complex in Class A β-Lactamases and Predict the Efficiency of Inhibi-
727 tion. Biochemistry. 2018 Jul; 57(26):3560–3563. https://pubs.acs.org/doi/10.1021/acs.biochem.8b00480, doi:
728 10.1021/acs.biochem.8b00480.

729 **Galdadas I**, Lovera S, Pérez-Hernández G, Barnes MD, Healy J, Afsharikho H, Woodford N, Bonomo RA, Ger-
730 vasio FL, Haider S. Defining the architecture of KPC-2 Carbapenemase: identifying allosteric networks
731 to fight antibiotics resistance. Scientific Reports. 2018 Dec; 8(1):12916. http://www.nature.com/articles/
732 s41598-018-31176-0, doi: 10.1038/s41598-018-31176-0.

733 **Glowacki DR**, Harvey JN, Mulholland AJ. Taking Ockham's razor to enzyme dynamics and catalysis. Nature
734 Chemistry. 2012 Mar; 4(3):169–176. http://www.nature.com/articles/nchem.1244, doi: 10.1038/nchem.1244.

735 **Gobeil SMC**, Ebert MCCJC, Park J, Gagné D, Doucet N, Berghuis AM, Pleiss J, Pelletier JN. The Structural Dynamics
736 of Engineered β-Lactamases Vary Broadly on Three Timescales yet Sustain Native Function. Scientific Reports.
737 2019 Dec; 9(1):6656. http://www.nature.com/articles/s41598-019-42866-8, doi: 10.1038/s41598-019-42866-8.

738 **Goddard TD**, Huang CC, Meng EC, Pettersen EF, Couch GS, Morris JH, Ferrin TE. UCSF ChimeraX: Meeting
739 modern challenges in visualization and analysis: UCSF ChimeraX Visualization System. Protein Science. 2018
740 Jan; 27(1):14–25. http://doi.wiley.com/10.1002/pro.3235, doi: 10.1002/pro.3235.

741 **Guillaume G**, Vanhove M, Lamotte-Brasseur J, Ledent P, Jamin M, Joris B, Frère JM. Site-directed Mutagen-
742 esis of Glutamate 166 in Two β-Lactamases: Kinetic and Molecular Modeling Studies. Journal of Biolog-
743 ical Chemistry. 1997 Feb; 272(9):5438–5444. http://www.jbc.org/lookup/doi/10.1074/jbc.272.9.5438, doi:
744 10.1074/jbc.272.9.5438.

745 **Hart KM**, Ho CMW, Dutta S, Gross ML, Bowman GR. Modelling proteins' hidden conformations to predict
746 antibiotic resistance. Nature Communications. 2016 Dec; 7(1):12965. http://www.nature.com/articles/
747 ncomms12965, doi: 10.1038/ncomms12965.

748 **Hermann JC**, Hensen C, Ridder L, Mulholland AJ, Höltje HD. Mechanisms of Antibiotic Resistance: QM/MM
749 Modeling of the Acylation Reaction of a Class A β-Lactamase with Benzylpenicillin. Journal of the Amer-
750 ican Chemical Society. 2005 Mar; 127(12):4454–4465. https://pubs.acs.org/doi/10.1021/ja044210d, doi:
751 10.1021/ja044210d.

752 **Hermann JC**, Ridder L, Höltje HD, Mulholland AJ. Molecular mechanisms of antibiotic resistance: QM/MM
753 modelling of deacylation in a class A β-lactamase. Org Biomol Chem. 2006; 4(2):206–210. http://xlink.rsc.
754 org/?DOI=B512969A, doi: 10.1039/B512969A.

755 **Hermann JC**, Ridder L, Mulholland AJ, Höltje HD. Identification of Glu166 as the General Base in the Acylation
756 Reaction of Class A β-Lactamases through QM/MM Modeling. Journal of the American Chemical Society.
757 2003 Aug; 125(32):9590–9591. https://pubs.acs.org/doi/10.1021/ja034434g, doi: 10.1021/ja034434g.

758 **Hester KP**, Bhattarai K, Jiang H, Agarwal PK, Pope C. Engineering Dynamic Surface Peptide Networks on Bu-
759 tyrylcholinesterase $_{G117H}$ for Enhanced Organophosphosphorus Anticholinesterase Catalysis. Chemical Re-
760 search in Toxicology. 2019 Sep; 32(9):1801–1810. https://pubs.acs.org/doi/10.1021/acs.chemrestox.9b00146,
761 doi: 10.1021/acs.chemrestox.9b00146.

762 **Hirvonen VHA**, Hammond K, Chudyk EI, Limb MAL, Spencer J, Mulholland AJ, van der Kamp MW. An Efficient
763 Computational Assay for β-Lactam Antibiotic Breakdown by Class A β-Lactamases. Journal of Chemical In-
764 formation and Modeling. 2019 Aug; 59(8):3365–3369. https://pubs.acs.org/doi/10.1021/acs.jcim.9b00442, doi:
765 10.1021/acs.jcim.9b00442.

766 **Horn JR**, Shoichet BK. Allosteric Inhibition Through Core Disruption. Journal of Molecular Biol-
767 ogy. 2004 Mar; 336(5):1283–1291. https://linkinghub.elsevier.com/retrieve/pii/S0022283604000221, doi:
768 10.1016/j.jmb.2003.12.068.

769 **Humphrey W**, Dalke A, Schulten K. VMD: Visual molecular dynamics. Journal of Molecular Graphics. 1996 Feb;
770 14(1):33–38. https://linkinghub.elsevier.com/retrieve/pii/0263785596000185, doi: 10.1016/0263-7855(96)00018-
771 5.

772 **Kamerlin SCL**, Warshel A. At the dawn of the 21st century: Is dynamics the missing link for understanding
773 enzyme catalysis? Proteins: Structure, Function, and Bioinformatics. 2010; p. NA–NA. http://doi.wiley.com/
774 10.1002/prot.22654, doi: 10.1002/prot.22654.

775 **Ke W**, Bethel CR, Papp-Wallace KM, Pagadala SRR, Nottingham M, Fernandez D, Buynak JD, Bonomo RA, van den
776 Akker F. Crystal Structures of KPC-2 β-Lactamase in Complex with 3-Nitrophenyl Boronic Acid and the Penam
777 Sulfone PSR-3-226. Antimicrobial Agents and Chemotherapy. 2012 May; 56(5):2713–2718. https://aac.asm.
778 org/content/56/5/2713, doi: 10.1128/AAC.06099-11.

779 **Laskowski RA**, Gerick F, Thornton JM. The structural basis of allosteric regulation in proteins.
780 FEBS Letters. 2009 Jun; 583(11):1692–1698. http://doi.wiley.com/10.1016/j.febslet.2009.03.019, doi:
781 10.1016/j.febslet.2009.03.019.

782 **Leung YC**, Robinson CV, Aplin RT, Waley SG. Site-directed mutagenesis of β-lactamase I: role of Glu-166. Bio-
783 chemical Journal. 1994 May; 299(3):671–678. https://portlandpress.com/biochemj/article/299/3/671/83575/
784 Sitedirected-mutagenesis-of-%CE%B2lactamase-I-role-of, doi: 10.1042/bj2990671.

785 **Liao Q**, Kulkarni Y, Sengupta U, Petrović D, Mulholland AJ, van der Kamp MW, Strodel B, Kamerlin SCL.
786 Loop Motion in Triosephosphate Isomerase Is Not a Simple Open and Shut Case. Journal of the Ameri-
787 can Chemical Society. 2018 Nov; 140(46):15889–15903. https://pubs.acs.org/doi/10.1021/jacs.8b09378, doi:
788 10.1021/jacs.8b09378.

789 **Luk LYP**, Javier Ruiz-Pernia J, Dawson WM, Roca M, Loveridge EJ, Glowacki DR, Harvey JN, Mulholland AJ, Tunon
790 I, Moliner V, Allemann RK. Unraveling the role of protein dynamics in dihydrofolate reductase catalysis.
791 Proceedings of the National Academy of Sciences. 2013 Oct; 110(41):16344–16349. http://www.pnas.org/cgi/
792 doi/10.1073/pnas.1312437110, doi: 10.1073/pnas.1312437110.

793 **Lythell E**, Suardíaz R, Hinchliffe P, Hanpaibool C, Visitsatthawong S, Oliveira ASF, Lang EJM, Surawatanawong P,
794 Lee VS, Rungrotmongkol T, Fey N, Spencer J, Mulholland AJ. Resistance to the "last resort" antibiotic colistin:
795 a single-zinc mechanism for phosphointermediate formation in MCR enzymes. Chemical Communications.
796 2020; 56(50):6874–6877. http://xlink.rsc.org/?DOI=D0CC02520H, doi: 10.1039/D0CC02520H.

797 **Maier JA**, Martinez C, Kasavajhala K, Wickstrom L, Hauser KE, Simmerling C. ff14SB: Improving the Accuracy
798 of Protein Side Chain and Backbone Parameters from ff99SB. Journal of Chemical Theory and Computation.
799 2015 Aug; 11(8):3696–3713. https://pubs.acs.org/doi/10.1021/acs.jctc.5b00255, doi: 10.1021/acs.jctc.5b00255.

800 **Mark P**, Nilsson L. Structure and Dynamics of the TIP3P, SPC, and SPC/E Water Models at 298 K. The Journal
801 of Physical Chemistry A. 2001 Nov; 105(43):9954–9960. https://pubs.acs.org/doi/10.1021/jp003020w, doi:
802 10.1021/jp003020w.

803 **Martínez L**. Automatic Identification of Mobile and Rigid Substructures in Molecular Dynamics Simulations
804 and Fractional Structural Fluctuation Analysis. PLOS ONE. 2015 Mar; 10(3):e0119264. https://dx.plos.org/10.
805 1371/journal.pone.0119264, doi: 10.1371/journal.pone.0119264.

806 **Mehta SC**, Rice K, Palzkill T. Natural Variants of the KPC-2 Carbapenemase have Evolved Increased Cat-
807 alytic Efficiency for Ceftazidime Hydrolysis at the Cost of Enzyme Stability. PLOS Pathogens. 2015
808 Jun; 11(6):e1004949. https://journals.plos.org/plospathogens/article?id=10.1371/journal.ppat.1004949, doi:
809 10.1371/journal.ppat.1004949, publisher: Public Library of Science.

810 **Meneksedag D**, Dogan A, Kanlikilicer P, Ozkirimli E. Communication between the active site and the allosteric
811 site in class A beta-lactamases. Computational Biology and Chemistry. 2013 Apr; 43:1–10. https://linkinghub.
812 elsevier.com/retrieve/pii/S147692711200093X, doi: 10.1016/j.compbiolchem.2012.12.002.

813 **Morin S**, Gagné SM. NMR Dynamics of PSE-4 β-Lactamase: An Interplay of ps-ns Order and µs-ms Motions in
814 the Active Site. Biophysical Journal. 2009 Jun; 96(11):4681–4691. https://linkinghub.elsevier.com/retrieve/pii/
815 S0006349509006997, doi: 10.1016/j.bpj.2009.02.068.

816 **Motlagh HN**, Wrabl JO, Li J, Hilser VJ. The ensemble nature of allostery. Nature. 2014 Apr; 508(7496):331–339.
817 http://www.nature.com/articles/nature13001, doi: 10.1038/nature13001.

818 **Naas T**, Oueslati S, Bonnin RA, Dabos ML, Zavala A, Dortet L, Retailleau P, Iorga BI. Beta-lactamase database
819 (BLDB) - structure and function. Journal of Enzyme Inhibition and Medicinal Chemistry. 2017 Dec; 32(1):917–
820 919. doi: 10.1080/14756366.2017.1344235.

821 **Oliveira ASF**, Shoemark DK, Campello HR, Wonnacott S, Gallagher T, Sessions RB, Mulholland AJ. Identification
822 of the Initial Steps in Signal Transduction in the α4β2 Nicotinic Receptor: Insights from Equilibrium and
823 Nonequilibrium Simulations. Structure. 2019 Jul; 27(7):1171–1183.e3. https://linkinghub.elsevier.com/retrieve/
824 pii/S0969212619301303, doi: 10.1016/j.str.2019.04.008.

825 **Oliveira ASF**, Teixeira VH, Baptista AM, Soares CM. Reorganization and Conformational Changes in the Reduc-
826 tion of Tetraheme Cytochromes. Biophysical Journal. 2005 Dec; 89(6):3919–3930. https://linkinghub.elsevier.
827 com/retrieve/pii/S0006349505730356, doi: 10.1529/biophysj.105.065144.

828 **Oliveira ASF**, Edsall CJ, Woods CJ, Bates P, Nunez GV, Wonnacott S, Bermudez I, Ciccotti G, Gallagher T, Sessions
829 RB, Mulholland AJ. A General Mechanism for Signal Propagation in the Nicotinic Acetylcholine Receptor
830 Family. Journal of the American Chemical Society. 2019 Dec; 141(51):19953–19958. https://pubs.acs.org/doi/
831 abs/10.1021/jacs.9b09055, doi: 10.1021/jacs.9b09055.

832 **Palzkill T**. Metallo-β-lactamase structure and function: Metallo-β-lactamase structure and function. Annals of
833 the New York Academy of Sciences. 2013 Jan; 1277(1):91–104. http://doi.wiley.com/10.1111/j.1749-6632.2012.
834 06796.x, doi: 10.1111/j.1749-6632.2012.06796.x.

835 **Palzkill T**. Structural and Mechanistic Basis for Extended-Spectrum Drug-Resistance Mutations in Altering the
836 Specificity of TEM, CTX-M, and KPC β-lactamases. Frontiers in Molecular Biosciences. 2018 Feb; 5:16. http:
837 //journal.frontiersin.org/article/10.3389/fmolb.2018.00016/full, doi: 10.3389/fmolb.2018.00016.

838 **Pan X**, He Y, Lei J, Huang X, Zhao Y. Crystallographic Snapshots of Class A β-Lactamase Catalysis Reveal Struc-
839 tural Changes That Facilitate β-Lactam Hydrolysis. Journal of Biological Chemistry. 2017 Mar; 292(10):4022–
840 4033. http://www.jbc.org/lookup/doi/10.1074/jbc.M116.764340, doi: 10.1074/jbc.M116.764340.

841 **Papp-Wallace KM**, Bethel CR, Distler AM, Kasuboski C, Taracila M, Bonomo RA. Inhibitor Resistance in the KPC-2
842 β-Lactamase, a Preeminent Property of This Class A β-Lactamase. Antimicrobial Agents and Chemotherapy.
843 2010 Feb; 54(2):890–897. https://AAC.asm.org/content/54/2/890, doi: 10.1128/AAC.00693-09.

844 **Papp-Wallace KM**, Taracila M, Wallace CJ, Hujer KM, Bethel CR, Hornick JM, Bonomo RA. Elucidating the role of
845 Trp105 in the KPC-2 β-lactamase: The Role of Trp105 in the KPC-2 β-Lactamase. Protein Science. 2010 Sep;
846 19(9):1714–1727. http://doi.wiley.com/10.1002/pro.454, doi: 10.1002/pro.454.

847 **Papp-Wallace KM**, Taracila MA, Smith KM, Xu Y, Bonomo RA. Understanding the Molecular Determinants of
848 Substrate and Inhibitor Specificities in the Carbapenemase KPC-2: Exploring the Roles of Arg220 and Glu276.
849 Antimicrobial Agents and Chemotherapy. 2012 Aug; 56(8):4428–4438. https://aac.asm.org/content/56/8/
850 4428, doi: 10.1128/AAC.05769-11.

851 **Pemberton OA**, Jaishankar P, Akhtar A, Adams JL, Shaw LN, Renslo AR, Chen Y. Heteroaryl Phosphonates as Noncovalent Inhibitors of Both Serine- and Metallocarbapenemases. Journal of Medicinal Chemistry. 2019 Sep; 62(18):8480–8496. https://pubs.acs.org/doi/10.1021/acs.jmedchem.9b00728, doi: 10.1021/acs.jmedchem.9b00728.

855 **Philippon A**, Slama P, Dény P, Labia R. A Structure-Based Classification of Class A β-Lactamases, a Broadly Diverse Family of Enzymes. Clinical Microbiology Reviews. 2016 Jan; 29(1):29–57. https://cmr.asm.org/content/29/1/29, doi: 10.1128/CMR.00019-15.

858 **Queenan AM**, Foleno B, Gownley C, Wira E, Bush K. Effects of Inoculum and -Lactamase Activity in AmpC- and Extended-Spectrum -Lactamase (ESBL)-Producing Escherichia coli and Klebsiella pneumoniae Clinical Isolates Tested by Using NCCLS ESBL Methodology. Journal of Clinical Microbiology. 2004 Jan; 42(1):269–275. http://jcm.asm.org/cgi/doi/10.1128/JCM.42.1.269-275.2004, doi: 10.1128/JCM.42.1.269-275.2004.

862 **Reinhard M**, Rüdiger M, Jockusch BM, Walter U. VASP interaction with vinculin: a recurring theme of interactions with proline-rich motifs. FEBS Letters. 1996 Dec; 399(1-2):103–107. http://doi.wiley.com/10.1016/S0014-5793%2896%2901295-1, doi: 10.1016/S0014-5793(96)01295-1.

865 **Roe DR**, Cheatham TE. PTRAJ and CPPTRAJ: Software for Processing and Analysis of Molecular Dynamics Trajectory Data. Journal of Chemical Theory and Computation. 2013 Jul; 9(7):3084–3095. https://pubs.acs.org/doi/10.1021/ct400341p, doi: 10.1021/ct400341p.

868 **Roy J**, Laughton CA. Long-Timescale Molecular-Dynamics Simulations of the Major Urinary Protein Provide Atomistic Interpretations of the Unusual Thermodynamics of Ligand Binding. Biophysical Journal. 2010 Jul; 99(1):218–226. https://linkinghub.elsevier.com/retrieve/pii/S0006349510004212, doi: 10.1016/j.bpj.2010.03.055.

872 **Salverda MLM**, De Visser JAGM, Barlow M. Natural evolution of TEM-1 β-lactamase: experimental reconstruction and clinical relevance. FEMS Microbiology Reviews. 2010 Nov; 34(6):1015–1036. https://academic.oup.com/femsre/article-lookup/doi/10.1111/j.1574-6976.2010.00222.x, doi: 10.1111/j.1574-6976.2010.00222.x.

875 **Savard PY**, Gagné SM. Backbone Dynamics of TEM-1 Determined by NMR: Evidence for a Highly Ordered Protein †. Biochemistry. 2006 Sep; 45(38):11414–11424. https://pubs.acs.org/doi/10.1021/bi060414q, doi: 10.1021/bi060414q.

878 **Singh P**, Abeysinghe T, Kohen A. Linking Protein Motion to Enzyme Catalysis. Molecules. 2015 Jan; 20(1):1192–1209. http://www.mdpi.com/1420-3049/20/1/1192, doi: 10.3390/molecules20011192.

880 **Stec B**, Holtz KM, Wojciechowski CL, Kantrowitz ER. Structure of the wild-type TEM-1 β-lactamase at 1.55 Å and the mutant enzyme Ser70Ala at 2.1 Å suggest the mode of noncovalent catalysis for the mutant enzyme. Acta Crystallographica Section D Biological Crystallography. 2005 Jul; 61(8):1072–1079. http://scripts.iucr.org/cgi-bin/paper?S0907444905014356, doi: 10.1107/S0907444905014356.

884 **Tomasello G**, Armenia I, Molla G. The Protein Imager: a full-featured online molecular viewer interface with server-side HQ-rendering capabilities. Bioinformatics. 2020 May; 36(9):2909–2911. https://academic.oup.com/bioinformatics/article/36/9/2909/5701652, doi: 10.1093/bioinformatics/btaa009.

887 **Tooke CL**, Hinchliffe P, Bonomo RA, Schofield CJ, Mulholland AJ, Spencer J. Natural variants modify Klebsiella pneumoniae carbapenemase (KPC) acyl–enzyme conformational dynamics to extend antibiotic resistance. Journal of Biological Chemistry. 2021; 296(17):100126. doi: 10.1074/jbc.ra120.016461.

890 **Tooke CL**, Hinchliffe P, Bragginton EC, Colenso CK, Hirvonen VHA, Takebayashi Y, Spencer J. β-Lactamases and β-Lactamase Inhibitors in the 21st Century. Journal of Molecular Biology. 2019 Aug; 431(18):3472–3500. https://linkinghub.elsevier.com/retrieve/pii/S0022283619301822, doi: 10.1016/j.jmb.2019.04.002.

893 **Wang J**, Wolf RM, Caldwell JW, Kollman PA, Case DA. Development and testing of a general amber force field. Journal of Computational Chemistry. 2004 Jul; 25(9):1157–1174. http://doi.wiley.com/10.1002/jcc.20035, doi: 10.1002/jcc.20035.

896 **Yigit H**, Queenan AM, Rasheed JK, Biddle JW, Domenech-Sanchez A, Alberti S, Bush K, Tenover FC. Carbapenem-Resistant Strain of Klebsiellaoxytoca Harboring Carbapenem-HydrolyzingB-LactamaseKPC-2. Antimicrobial Agents and Chemotherapy. 2003 Dec; 47(12):3881–3889. https://AAC.asm.org/content/47/12/3881, doi: 10.1128/AAC.47.12.3881-3889.2003.

900 **Zaccolo M**, Gherardi E. The effect of high-frequency random mutagenesis on in vitro protein evolution: a study on TEM-1 β-lactamase 1 1Edited by A. R. Fersht. Journal of Molecular Biology. 1999 Jan; 285(2):775–783. https://linkinghub.elsevier.com/retrieve/pii/S0022283698922628, doi: 10.1006/jmbi.1998.2262.

Zawadzke LE, Chen CCH, Banerjee S, Li Z, Wäsch S, Kapadia G, Moult J, Herzberg O. Elimination of the Hydrolytic Water Molecule in a Class A β-Lactamase Mutant: Crystal Structure and Kinetics. Biochemistry. 1996 Jan; 35(51):16475–16482. https://pubs.acs.org/doi/10.1021/bi962242a, doi: 10.1021/bi962242a.

Zondlo NJ. Aromatic–Proline Interactions: Electronically Tunable CH/π Interactions. Accounts of Chemical Research. 2013 Apr; 46(4):1039–1049. https://pubs.acs.org/doi/10.1021/ar300087y, doi: 10.1021/ar300087y.

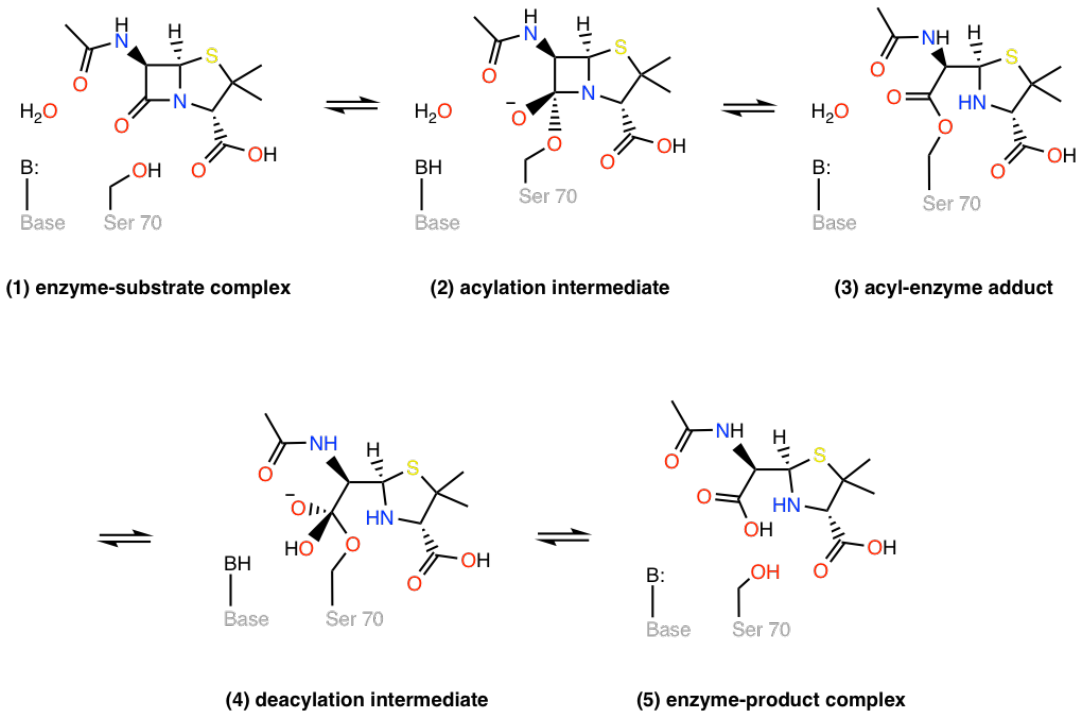

Figure 1–Figure supplement 1. Catalytic cycle of a class A β-lactamase illustrated on the core structure of penicillins. Class A β-lactamases use an active site serine nucleophile to cleave the β-lactam bond of the substrate in a two-step acylation-deacylation reaction cycle that leads to overall hydrolysis. (1) The acylation reaction initiates with the reversible binding of the antibiotic in the active site and the formation of the enzyme-substrate complex. In the next step, a general base-catalyzed nucleophilic attack on the β-lactam carbonyl by the serine hydroxyl takes place through a tetrahedral intermediate (2) to form a transient acyl-enzyme adduct (3). In the deacylation step, the acyl-enzyme adduct (3) undergoes a general base-catalyzed attack by a hydrolytic water molecule to form a second tetrahedral intermediate (4), which then forms a postcovalent product complex (5), from which the hydrolyzed product is released.

Secondary Structure	Residues			
	TEM-1 (PDB id 1PZP)	TEM-1 Mutations	KPC-2 (PDB id 6D18)	KPC-2 Mutations
α_1	26-40	H26, E28, D35, D38, Q39, L40,	26-40	
α_1-β_1	41-42	G41, A42	41-42	
β_1	43-50		43-50	
β_1-β_2	51-55		51-55	
β_2	56-60	L57	56-60	
β_2-β_3	61-65		61-65	
β_3	66-67		66-67	
β_3-α_2	68-71		68-70	
α_2	72-85		72-87	
α_2-β_4	86-93	Q90, G92	88-93	D92, T93
β_4	94-95		94-95	
β_4-α_3	96-97		96-97	
α_3	98-101	Q99, N100,	98-102	
α_3-turn-α_4	102-107	E104, Y105, S106	103-107	P104, W105
α_4	108-111		108-113	
α_4-β_5	112-116	T114, D115	114-116	
β_5	117-118		117-118	
α_5	119-129		119-129	
α_5-α_6	130-131		130	
α_6	132-142		131-142	
α_6-α_7	143-144		143-144	
α_7	145-154	H153	145-155	G147
α_7-α_8	155-166	M155, G156, D157, H158	156-166	
α_8	167-171		167-171	L169
Ω	172-179	I173, N175, D176	172-179	A172, D179
β_6	180-181		180-181	
β_6-α_9	182		182	
α_9	183-195		183-195	
α_9-α_{10}	196-200	G196	196-199	
α_{10}	201-212	R204,	200-213	P202
Hinge	213-218	G218	214-218	
α_{11}	219-224	L220, L221, S223, A224	219-225	
α_{11}-β_7	225-229		226-229	
β_7	230-237	F230	230-237	
β_7-β_8	238-243	G238, E240	238-243	V240, Y241, G242, T243
β_8	244-251		244-251	
β_8-β_9	252-258		252-258	T253
β_9	259-266		259-266	
β_9-α_{12}	267-272	G267, S268, A270, T271,	267-273	
α_{12}	273-288	R275, N276, I279, A280, A284	274-287	H274

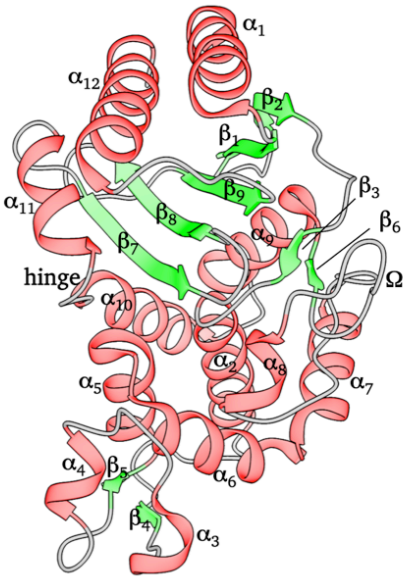

Figure 1–Figure supplement 2. The loops are named based on the secondary structure it connects. For example, loop α1-β1 connects α1 helix and β1 sheet. It must be noted that the boundaries of the secondary structure are approximate and may vary by ±2 residues based on the visualization software used. This work employed ChimeraX to define secondary structure. The mutations listed are those that fall on the communication pathway.

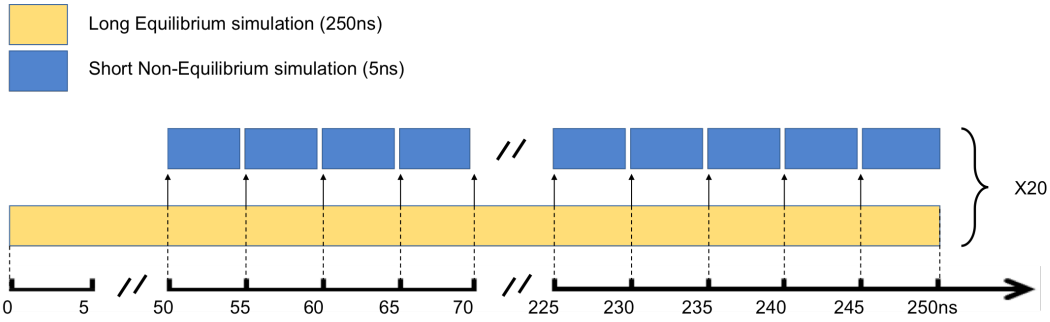

Figure 2–Figure supplement 1. Schematic description of the long equilibrium (EQ) and short nonequilibrium (NE) simulations. 20 replicates of IB_{EQ} simulations were run starting from the minimized crystal structure. From the equilibrated part of each replica (50 ns onwards), the final conformation of the protein-ligand complex was extracted at every 5 ns, the perturbation (removal of the ligand) was introduced, and a short Apo_{NE} simulations was run for 5 ns. In total, 800 Apo_{NE} simulations were performed for each system. In addition to these simulations, 20 replicas of the Apo_{EQ} were also simulated.

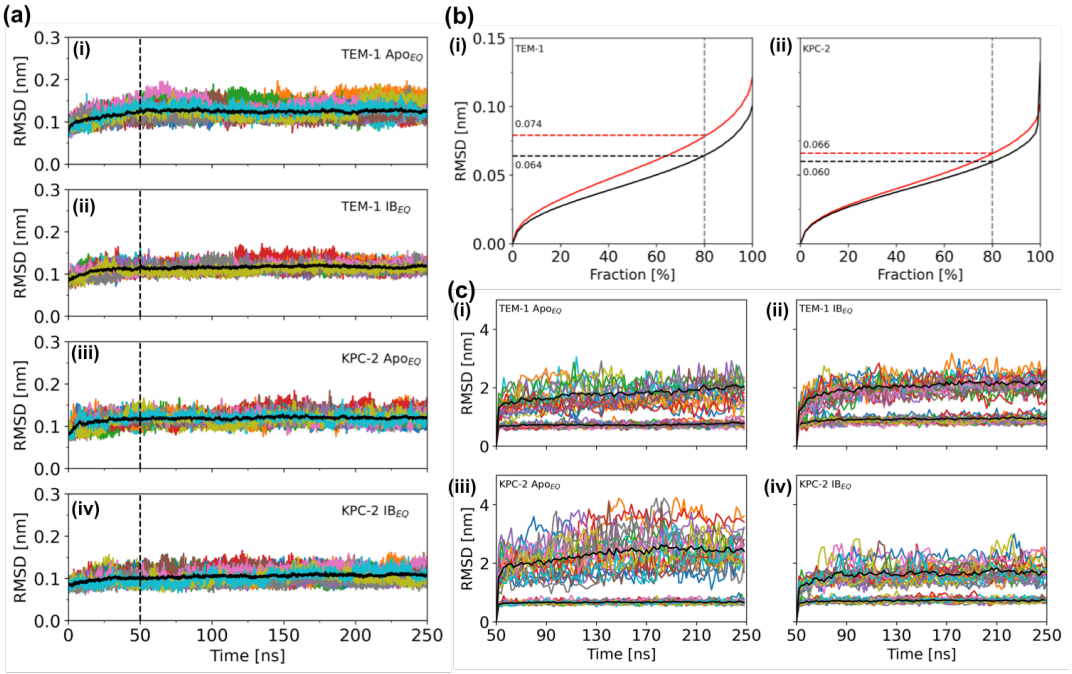

Figure 2–Figure supplement 2. (a) Time series of the Cα Root Mean Squared Deviation (RMSD) of (ai) TEM-1 Apo_{EQ}, (aii) TEM-1 IB_{EQ}, (aiii) KPC-2 Apo_{EQ} and (aiv) KPC-2 IB_{EQ} systems, measured over the course of the 250 ns of each replica. The black line represents the average of the 20 replicates. (b) RMSD calculated as a function of the fraction of the total Cα atoms considered for structural alignment in (i) TEM-1 and (ii) KPC-2. The plots indicate that 80% of conformations in TEM-1 that can be aligned to below 0.064 nm (Apo_{EQ}; black) and 0.074 nm (IB_{EQ}; red). Similarly, in KPC-2, 80% of the conformations could be superimposed to below 0.060 nm (Apo_{EQ}; black) and 0.066 nm (IB_{EQ}; red). This constitutes the core of the enzyme. (c) Fractional Cα RMSD calculated after identification of the core in (ci) TEM-1 Apo_{EQ} (cii) TEM-1 IB_{EQ} (ciii) KPC-2 Apo_{EQ} (civ) KPC-2 IB_{EQ}. The bottom black line denotes the stable core and consists of 80% Cα atoms. The top black line is the average of the remainder 20% Cα atoms calculated from all 20 replicates. These constitute the non-core Cα atoms that display deviation in all simulations.

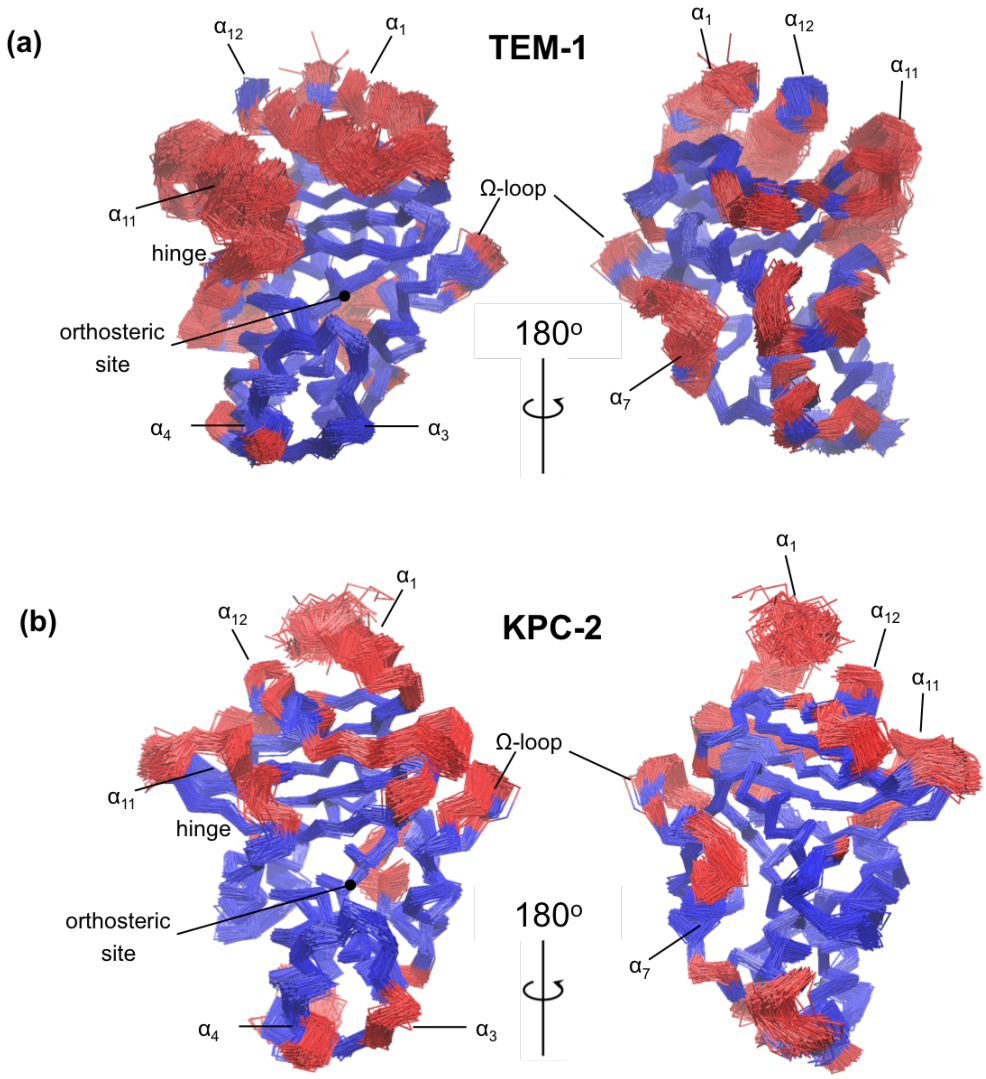

Figure 2–Figure supplement 3. Core Cα RMSD superimposition from (a) TEM-1 and (b) KPC-2 IB_{EQ} simulations. The structural alignment was calculated from the equilibrated section of all IB_{EQ} trajectories and rendered to illustrate 100 uniformly separated frames. The least mobile Cα atoms are colored blue and the most mobile atoms (red) provide the structural basis for the differential RMSDs.

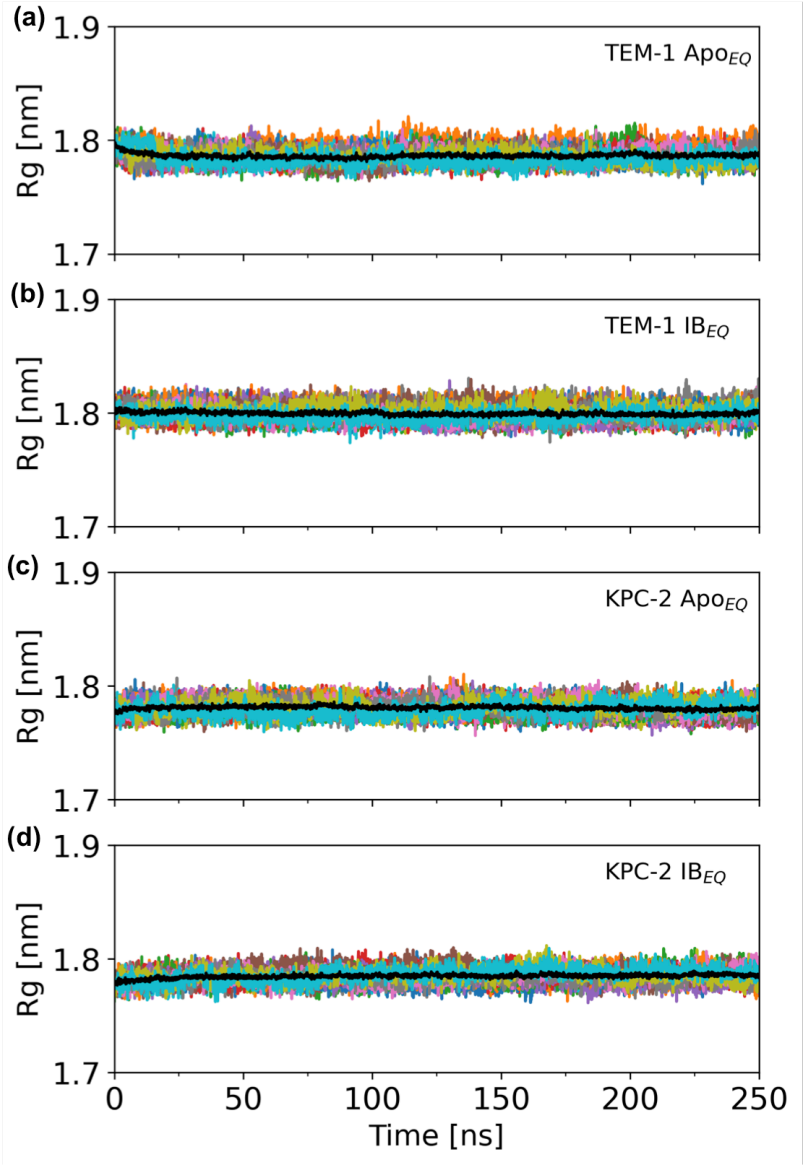

Figure 2–Figure supplement 4. Time evolution of the radius of gyration (Rg) of the complete (a) TEM-1 Apo$_{EQ}$, (b) TEM-1 IB$_{EQ}$, (c) KPC-2 Apo$_{EQ}$ and (d) KPC-2 IB$_{EQ}$ enzymes, measured over the course of the 250 ns of each replicate. The black line represents the average of 20 replicates.

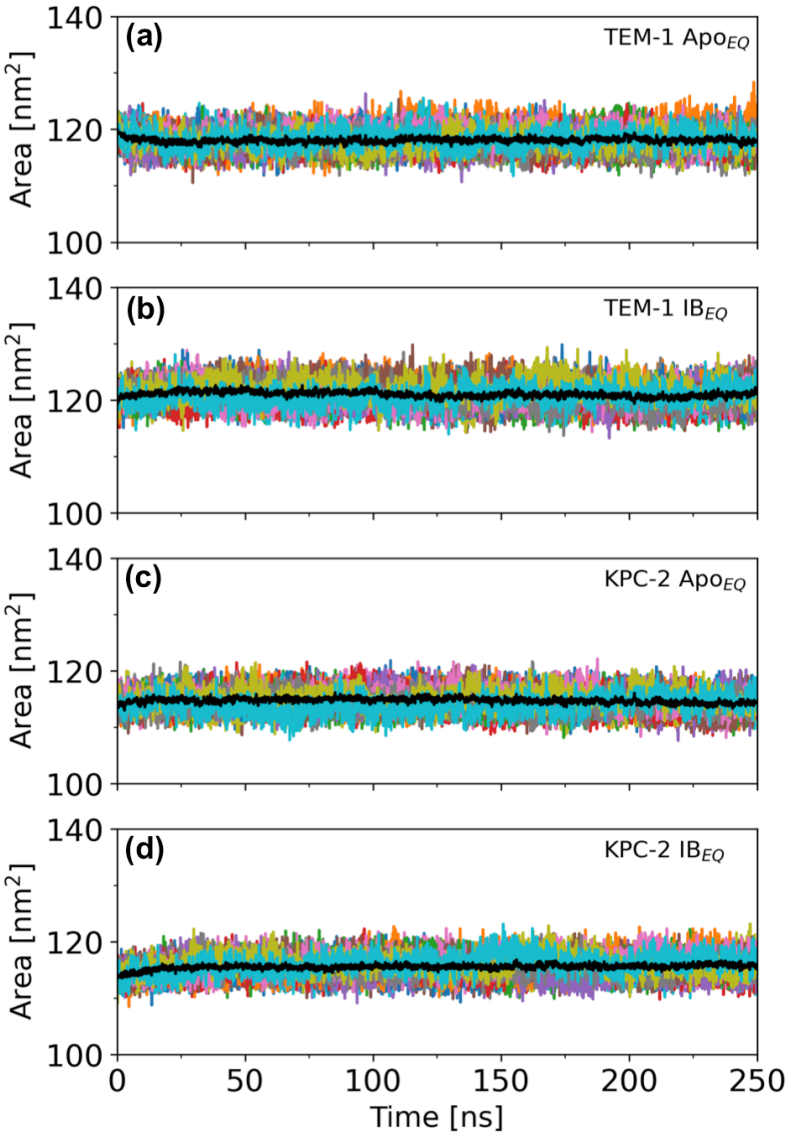

Figure 2–Figure supplement 5. Solvent accessible surface area (SASA) was calculated to assess structural distortion in the complete (a) TEM-1 Apo_{EQ}, (b) TEM-1 IB_{EQ}, (c) KPC-2 Apo_{EQ} and (d) KPC-2 IB_{EQ} enzymes, measured over the course of the 250 ns of each replicate. The black line represents the average of 20 replicates.

Property	System		Value
RMSD	TEM-1	Apo_{EQ}	0.12 nm
		IB_{EQ}	0.11 nm
	KPC-2	Apo_{EQ}	0.12 nm
		IB_{EQ}	0.10 nm
Rg	TEM-1	Apo_{EQ}	1.78 nm
		IB_{EQ}	1.79 nm
	KPC-2	Apo_{EQ}	1.78 nm
		IB_{EQ}	1.78 nm
SASA	TEM-1	Apo_{EQ}	118 nm^2
		IB_{EQ}	121 nm^2
	KPC-2	Apo_{EQ}	114 nm^2
		IB_{EQ}	115 nm^2

Figure 2–Figure supplement 6. Dynamical properties (RMSD, Rg and SASA) used to assess structural stability of the systems over the course of the equilibrium simulation. The values represent the averages calculated from the equilibrated part (50-250 ns) of all 20 replicate simulations of each system.

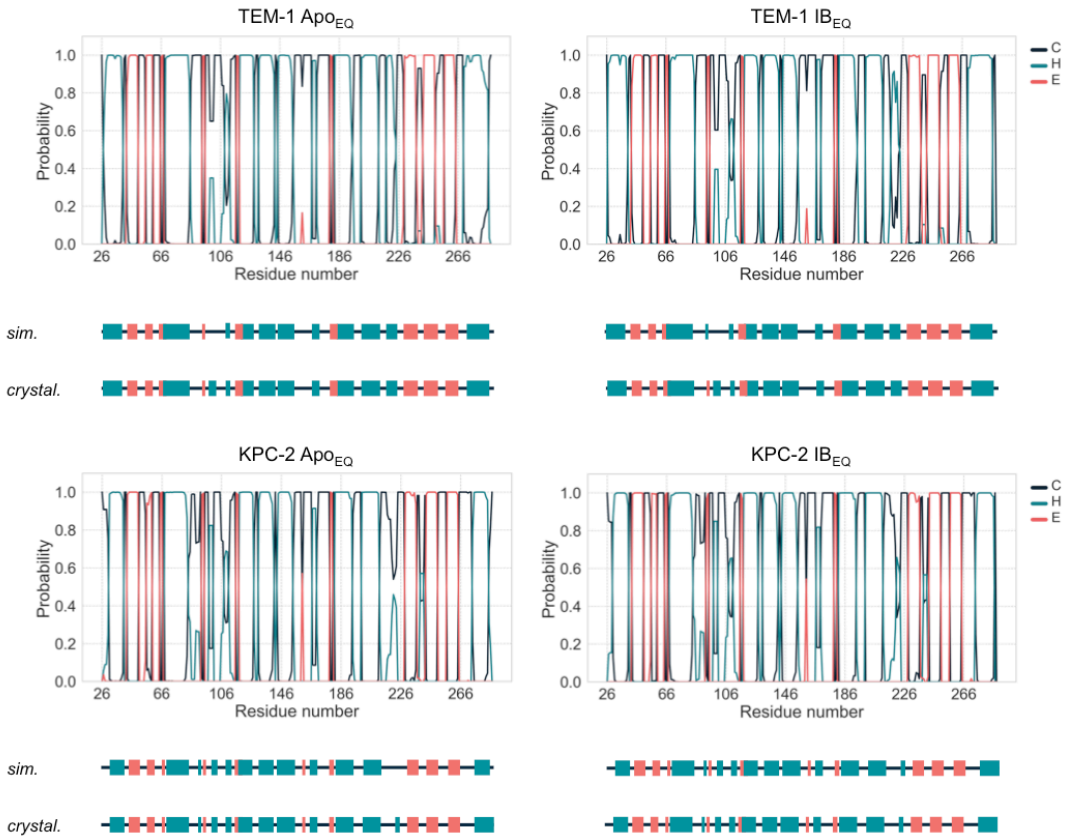

Figure 2–Figure supplement 7. Probability to find each residue in a coil ('C'), helix ('H'), or strand ('E'). The secondary structure element was assigned to each residue in each frame of each of the 20 replicas per system using the DSSP algorithm as implemented in MDTraj python library. The secondary structure of TEM-1 and KPC-2 as assigned from the crystal structure (*cryst.*), as well as the most probable assignment according to the simulations (*sim.*) is depicted as a cartoon below each plot.

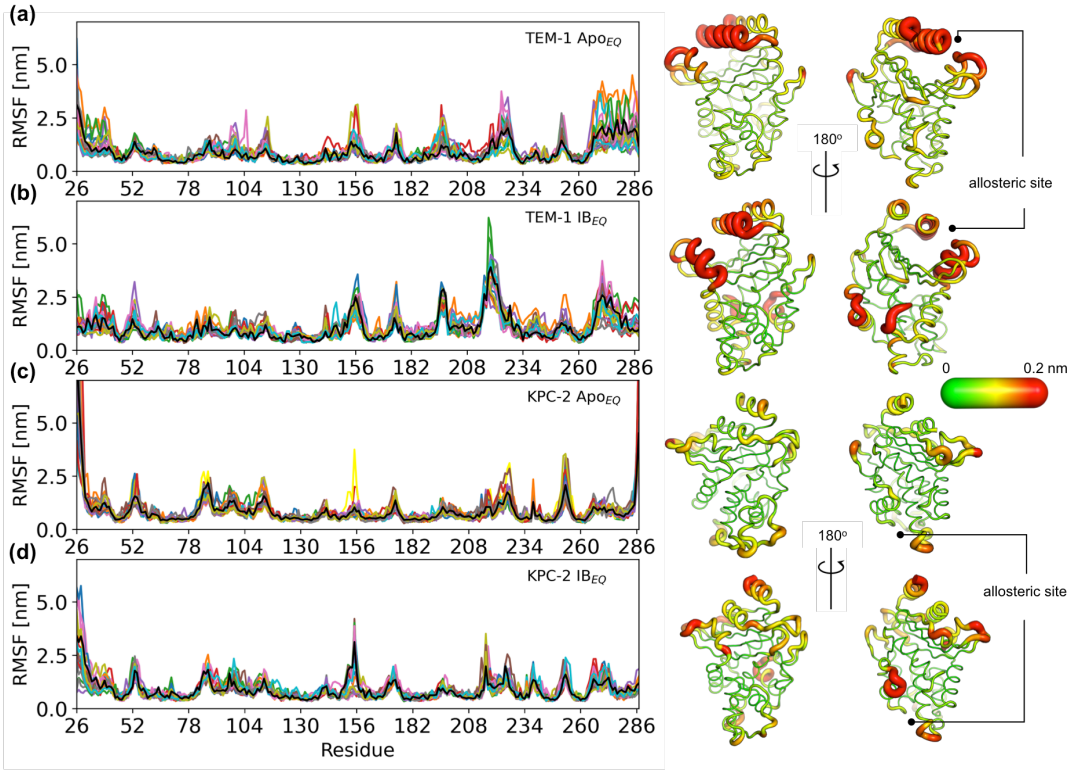

Figure 3–Figure supplement 1. Positional C Root Mean Square Fluctuation (RMSF) of (a) TEM-1 Apo$_{EQ}$, (b) TEM-1 IB$_{EQ}$, (c) KPC-2 Apo$_{EQ}$ and (d) KPC-2 IB$_{EQ}$ systems. The black line represents the average RMSF calculated from the last 200 ns of all 20 replicate simulations. This average value is mapped on the structure to highlight regions of high flexibility.

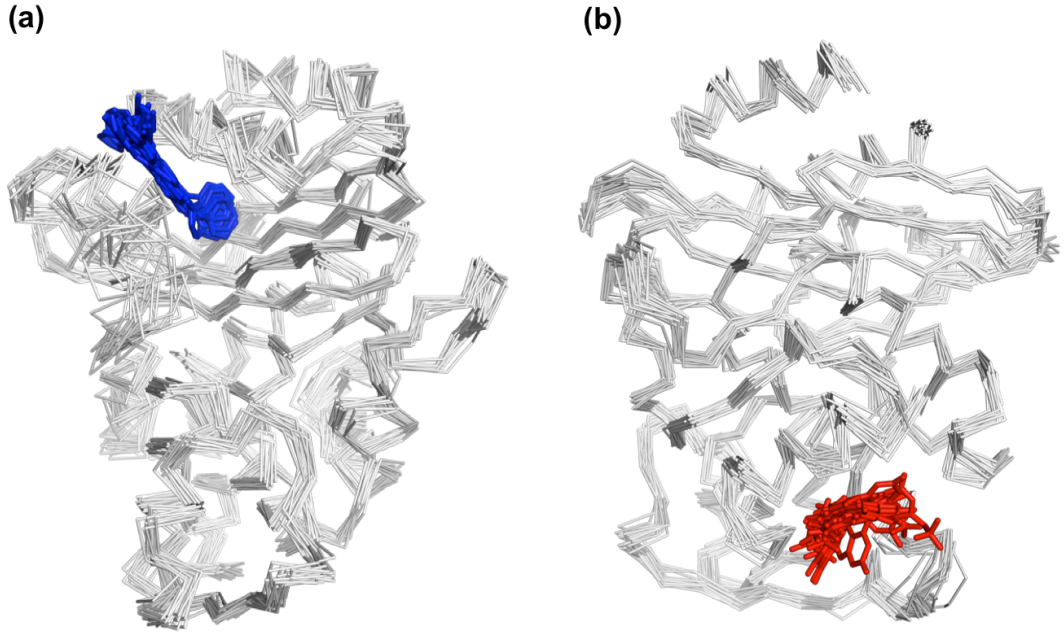

Figure 3–Figure supplement 2. Snapshot of the last frame from (a) TEM-1 IB$_{EQ}$ and (b) KPC-2 IB$_{EQ}$ replicate simulations, highlighting the spatial position of the ligands in the allosteric binding sites. FTA is represented as blue sticks and GTV is colored in red.

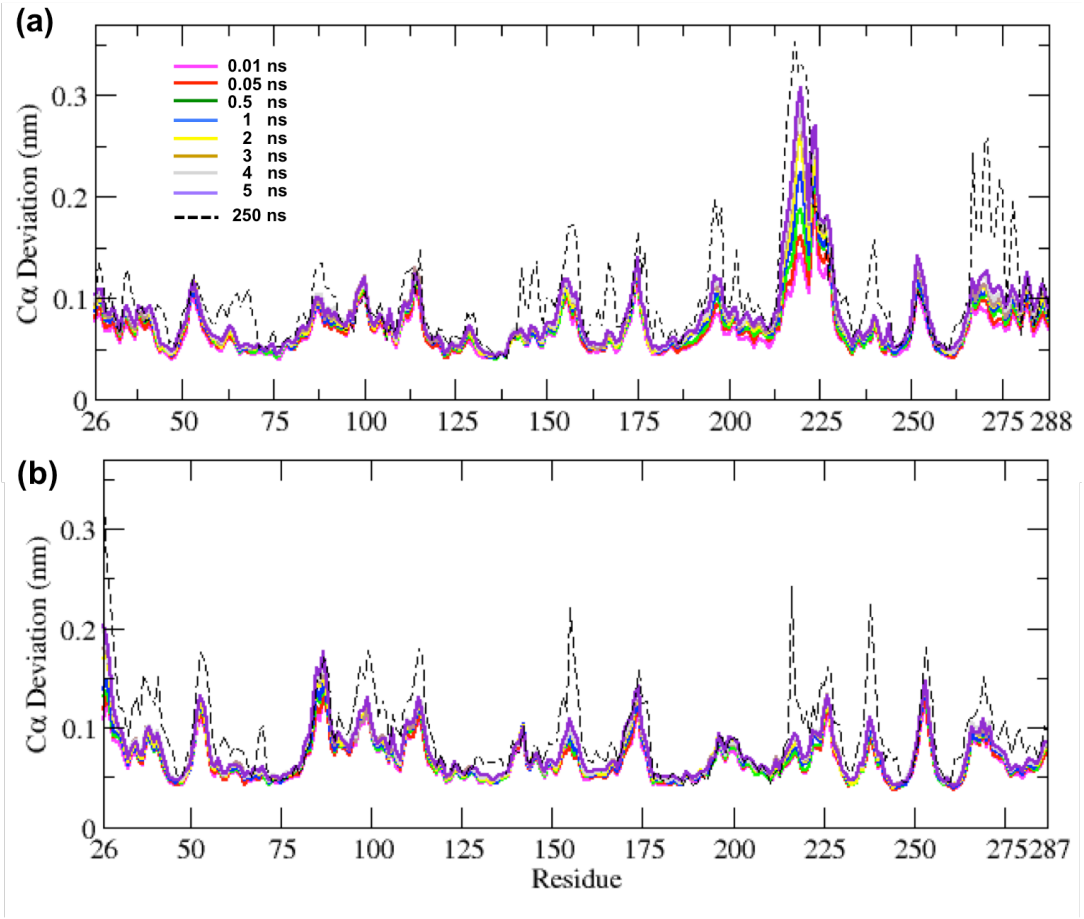

Figure 3–Figure supplement 3. Average Cα deviation between the IB_{EQ} and Apo_{NE} calculated using the subtraction method for (a) TEM-1 and (b) KPC-2. Average from all 800 simulations at various time points are illustrated. The average Cα deviation between the IB_{EQ} and Apo_{NE} simulations is plotted as a dotted line for comparison.

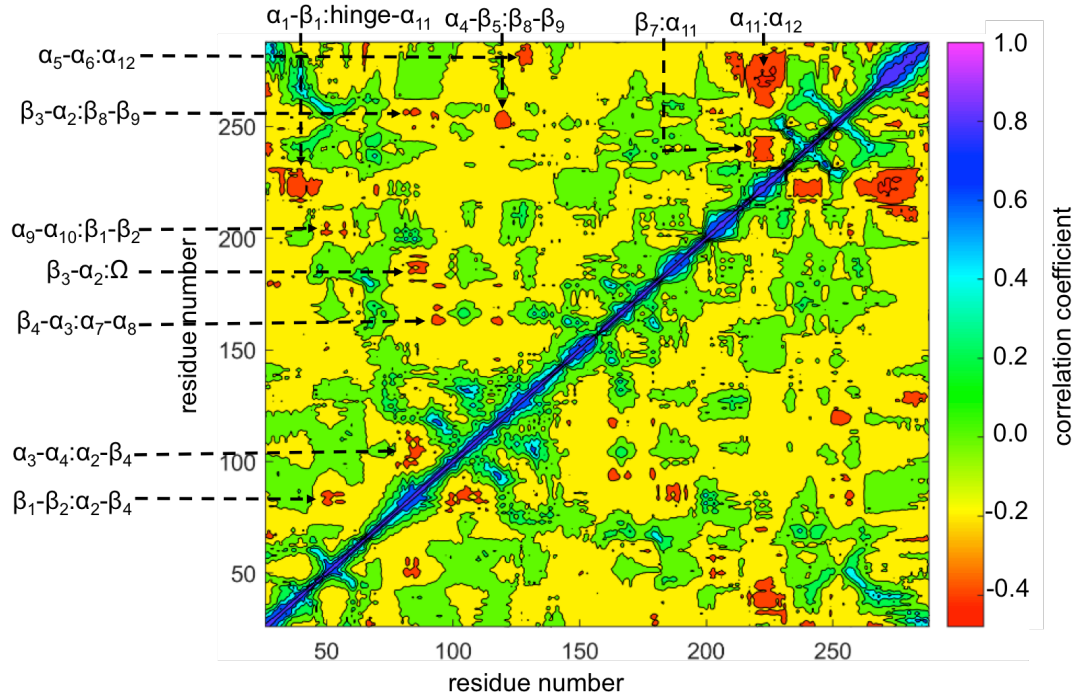

Figure 5–Figure supplement 1. TEM-1 averaged DCCM computed from all nonequilibrium trajectories. The regions showing significant correlations are identified: β1-β2:α2-β4, α3-α4:α2-β4, β4-α3:α7-α8, β3-α2:Ω, α9-α10:β1-β2, β3-α2:β8-β9, α5-α6:α12, α1-β1:hinge-α11, α4-β5:β8-β9, β7:α11 and α11:α12.

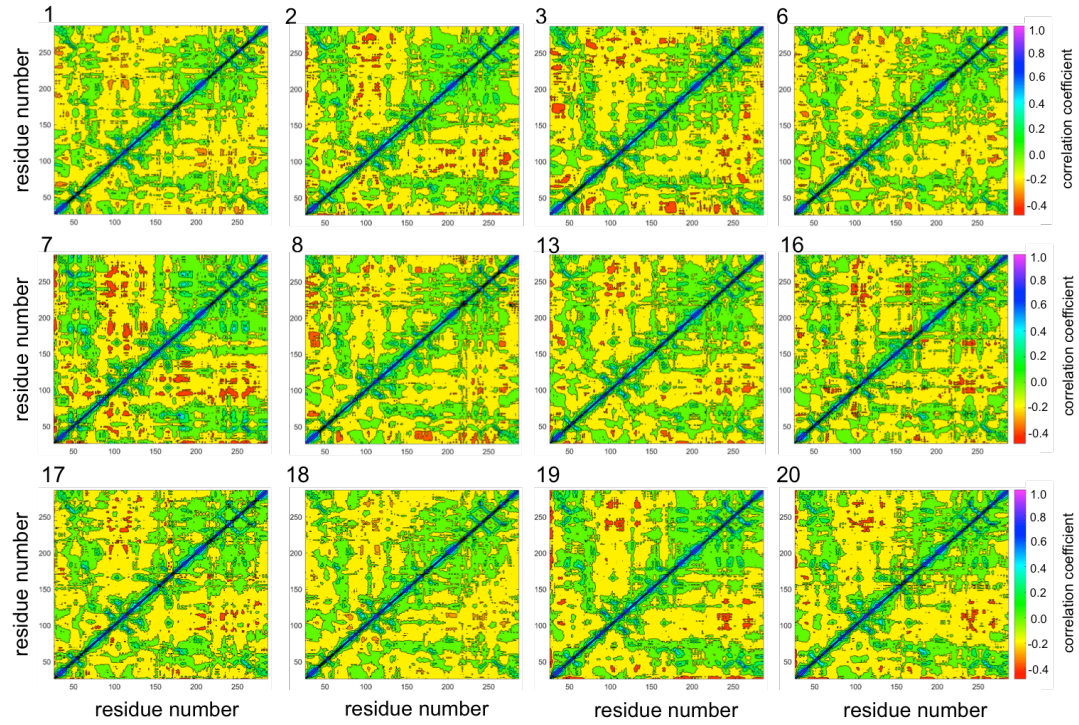

Figure 5–Figure supplement 2. Selected DCCMs computed for individual 5 ns nonequilibrium MD trajectories of KPC-2. These individual trajectories show different behavior from the averaged results (see Figure 5), as these trajectories show several regions of significant correlations similar to the TEM-1 nonequilibrium DCCM.

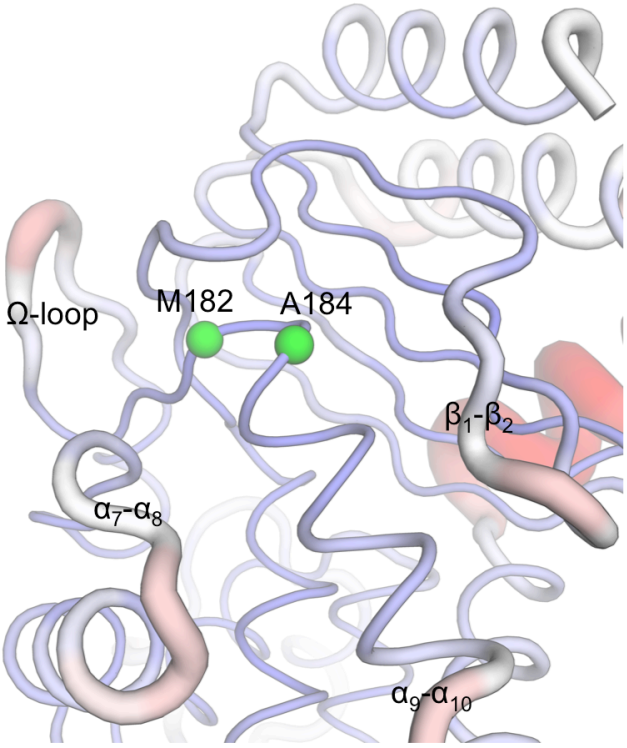

Figure 6–Figure supplement 1. Spatial position of M182 and A184 on TEM-1. These residues (green spheres) are not on the communication pathway per se; but are in close vicinity and surrounded by the Ω loop, α7-α8 loop, β1-β2 loop and α9-α10 loop, that are involved in the communication network.